

Manuscript Number: NIMG-18-2542R1

Title: Age-related microstructural and physiological changes in normal brain measured by MRI γ -metrics derived from anomalous diffusion signal representation

Article Type: VSI: Imaging Brain Aging

Section/Category: Cognition/Aging

Corresponding Author: Mr. Michele Guerreri, MSc

Corresponding Author's Institution: Sapienza University

First Author: Michele Guerreri, MSc

Order of Authors: Michele Guerreri, MSc; Marco Palombo; Alessandra Caporale; Fabrizio Fasano; Emiliano Macaluso; Marco Bozzali; Silvia Capuani

Abstract: Nowadays, increasing longevity associated with declining cerebral nervous system functions, suggests the need for continued development of new imaging contrast mechanisms to support the differential diagnosis of age-related decline.

In our previous papers, we developed a new imaging contrast metrics derived from anomalous diffusion signal representation and obtained from diffusion-weighted (DW) data collected by varying diffusion gradient strengths. Recently, we highlighted that the new metrics, named γ -metrics, depended on the local inhomogeneity due to differences in magnetic susceptibility between tissues and diffusion compartments in young healthy subjects, thus providing information about myelin orientation and iron content within cerebral regions. The major structural modifications occurring in brain aging are myelinated fibers damage in nerve fibers and iron accumulation in gray matter nuclei. Therefore, we investigated the potential of γ -metrics in relation to other conventional diffusion metrics such as DTI, DKI and NODDI in detecting age-related structural changes in white matter (WM) and subcortical gray matter (scGM). DW-images were acquired in 32 healthy subjects, adults and elderly (age range 20 to 77 years) using 3.0T and 12 b-values up to 5000s/mm². Association between diffusion metrics and subjects' age was assessed using linear regression. A decline in mean γ ($M\gamma$) in the scGM and a complementary increase in radial γ (γ_{\perp}) in frontal WM, genu of corpus callosum and anterior corona radiata with advancing age were found. We suggest that the increase in γ_{\perp} may reflect declined myelin density, and $M\gamma$ decrease may mirror iron accumulation. An increase in $D//$ and a decrease in the orientation dispersion index (ODI) were associated with axonal loss in the pyramidal tracts, while their inverted trends within the thalamus were thought to be linked to reduced architectural complexity of nerve fibers. γ -metrics together with conventional diffusion-metrics can more comprehensively characterize the complex mechanisms underlining age-related changes than conventional diffusion techniques alone.

1 **Age-related microstructural and physiological changes in normal brain measured by MRI γ -**
2 **metrics derived from anomalous diffusion signal representation**

3
4
5
6 Michele Guerrieri^{a,b*}, Marco Palombo^{b,c}, Alessandra Caporale^{b,d}, Fabrizio Fasano^e, Emiliano
7 Macaluso^f, Marco Bozzali^g, and Silvia Capuani^{b,g}

8
9 ^a*SAIMLAL department, Sapienza, Piazzale Aldo Moro, 5, 00185 Roma RM, Italy*

10 ^b*Institute for Complex Systems, CNR, Rome, Italy*

11 ^c*Department of Computer Science & Centre for Medical Image Computing, University College*
12 *London, London, United Kingdom*

13 ^d*Laboratory for Structural, Physiologic and Functional Imaging, Perelman School of Medicine*
14 *University of Pennsylvania, Philadelphia, PA, USA.*

15 ^e*Department of Neuroscience, Parma University, Parma, Italy*

16 ^f*ImpAct Team, Lyon Neuroscience Research Center, Lyon, France*

17 ^g*Neuroimaging Laboratory, Santa Lucia Foundation, Rome, Italy*

18
19 October 13, 2018

20
21
22
23
24
25
26
27
28
29
30 *Corresponding author: Michele Guerrieri

31 Fermi building, Department of Physics, Sapienza University of Rome, Piazzale Aldo Moro, 5,
32 00185 Rome, Italy.

33 E-mail address: michele.guerrieri@gmail.com

Highlights

γ metrics provides complementary information compared to conventional diffusion metrics
This study shows the added value of γ -metrics to assess brain alterations due to aging
Axial γ increases in white matter may reflect breakdown of myelin and axonal damage
Mean γ decrease in subcortical gray matter may mirror iron deposit accumulation.

Abstract

Nowadays, increasing longevity associated with declining cerebral nervous system functions, suggests the need for continued development of new imaging contrast mechanisms to support the differential diagnosis of age-related decline.

In our previous papers, we developed a new imaging contrast metrics derived from anomalous diffusion signal representation and obtained from diffusion-weighted (DW) data collected by varying diffusion gradient strengths. Recently, we highlighted that the new metrics, named γ -metrics, depended on the local inhomogeneity due to differences in magnetic susceptibility between tissues and diffusion compartments in young healthy subjects, thus providing information about myelin orientation and iron content within cerebral regions. The major structural modifications occurring in brain aging are myelinated fibers damage in nerve fibers and iron accumulation in gray matter nuclei. Therefore, we investigated the potential of γ -metrics in relation to other conventional diffusion metrics such as DTI, DKI and NODDI in detecting age-related structural changes in white matter (WM) and subcortical gray matter (scGM). DW-images were acquired in 32 healthy subjects, adults and elderly (age range 20 to 77 years) using 3.0T and 12 b-values up to 5000s/mm². Association between diffusion metrics and subjects' age was assessed using linear regression. A decline in mean γ ($M\gamma$) in the scGM and a complementary increase in radial γ (γ_{\perp}) in frontal WM, genu of corpus callosum and anterior corona radiata with advancing age were found. We suggest that the increase in γ_{\perp} may reflect declined myelin density, and $M\gamma$ decrease may mirror iron accumulation. An increase in $D_{//}$ and a decrease in the orientation dispersion index (ODI) were associated with axonal loss in the pyramidal tracts, while their inverted trends within the thalamus were thought to be linked to reduced architectural complexity of nerve fibers. γ -metrics together with conventional diffusion-metrics can more comprehensively characterize the complex mechanisms underlining age-related changes than conventional diffusion techniques alone.

69 **Keywords:** Normal aging, Brain, DTI, DKI, NODDI, Anomalous diffusion, Iron deposition

70 **1 Introduction**

71 The human brain undergoes regional-specific structural and physiological changes during lifespan,
72 which are reflected in a decline in cognitive abilities that become less and less efficient with aging
73 (Lockhart et al., 2014). Axonal damage and disintegration, loss of neuronal cells, myelin
74 degradation and iron accumulation (Draganski et al., 2011, Xu et al., 2008, Ashraf et al., 2018) are
75 the main age-related modifications that inexorably occur in the aging brain. With increasing life
76 expectancy in developed countries, there is a great need to establish efficient protocols for the early
77 diagnosis of cerebral decline that can support the development of new drugs and new therapies for
78 both normal and pathological aging.

79 In the last decades, magnetic resonance diffusion imaging (MRI) techniques and in particular
80 diffusion tensor imaging (DTI) studies (Basser et al., 1994) have contributed to the neuroscience of
81 normal ageing and to characterizing changes in morphology and tissues that occur with advancing
82 age. From the fourth decade of life, DTI metrics highlight a decline in fractional anisotropy (FA)
83 and a complementary increase in mean diffusivity (MD) in cerebral white matter (WM) due to
84 aging (Salat et al., 2005). This behavior of the DTI parameters reflects loss of WM fibers and of
85 their directionality and a reduction in axonal diameters (Bartzokis et al., 2012, Callaghan et al.,
86 2014). On the other hand, DTI investigations into cerebral gray matter (GM) as a function of
87 subjects' age, showed less clear patterns (Rathi et al., 2014, Salminen et al., 2016), whereas T1, T2
88 and T2* weighted imaging and susceptibility-based imaging studies highlighted GM atrophy
89 together with an increase in iron content in specific GM regions (Pfefferbaum et al., 2010, Haacke
90 et al., 2010, Daugherty and Raz, 2015, Pirpamer et al., 2016). DTI parameters quantify the diffusive
91 properties of bulk water poorly interacting with the complex structure of the neural tissue, so DTI
92 metrics have a limited sensitivity and specificity in the detection of early microstructural changes in
93 WM and GM. Moreover, the evaluation of early physiological modification due to different iron
94 content in vivo is challenging and still requires further investigation (Pfefferbaum et al., 2010). As a
95 consequence, in the last few years, several methods have been developed to increase the potential
96 ability of MRI diffusion techniques in detecting rearrangement of WM and its modification due to
97 normal and pathological aging, each with its strengths and weaknesses (Jelescu and Budde, 2017).
98 Two complementary approaches have emerged for extracting information on the tissue
99 microstructure exploiting the biological water diffusion signal: signal representation and
100 biophysical tissue modeling (Jelescu and Budde, 2017; Novikov et al. 2018). On the one hand,
101 signal representation or “statistical models” such as DTI and diffusion kurtosis imaging (DKI)
102 quantify parameters deriving from statistical mechanics without assumptions about the underlying

103 tissue, but they lack specificity, and provide only an indirect characterization of the microstructure
104 (Kiselev, 2017). On the other hand, biophysical tissue models such as neurite orientation
105 distribution and density imaging (NODDI) require schematic-geometric assumptions about the
106 underlying tissues. Therefore, even if such models can potentially provide greater specificity and
107 interpretation of biologically relevant parameters, the results are dramatically dependent on the
108 initial geometric assumptions that in general may not well describe the main components of tissue
109 microstructures, especially their changes due to pathologies (Novikov et al., 2018). Since DKI is
110 sensitive to water molecules which interact more with the cerebral microstructures than those of
111 bulk water considered in DTI, Kurtosis techniques have been used to study healthy aging as an
112 extension of DTI as these techniques are more sensitive to microstructural changes (Coutu et al.
113 2014; Gong et al. 2014; Lätt et al. 2013).

114
115 In parallel, several strategies have been developed to quantify the differences in magnetic
116 susceptibility ($\Delta\chi$) in brain tissues that potentially offer the possibility to measure the presence of
117 heavy metals, such as iron in GM and WM, and to highlight the directionality, the micro-
118 architecture and the chemical arrangement of the neural tissues. As an example, quantitative
119 susceptibility mapping (QSM) allows the calculation of bulk magnetic susceptibility distribution of
120 tissues in vivo from gradient echo (GRE) magnetic resonance phase images (Langkammer et al.,
121 2012) while susceptibility tensor imaging (STI) quantifies the amount of $\Delta\chi$ anisotropy (Liu, 2010).
122 However, in order to compute the susceptibility tensor, it is necessary to acquire the signal along at
123 least six different orientations of the sample with respect to the static magnetic field (B_0) (Liu,
124 2010). This is an intrinsic limitation of STI imaging, since subject rotation during acquisition is
125 hardly practicable in clinical applications.

126 Recently, we showed the potential of the new γ -metrics derived from anomalous diffusion (AD)
127 signal representation in highlighting $\Delta\chi$ in myelin orientation and iron contents within selected
128 regions of WM and subcortical GM (scGM), respectively (Caporale et al., 2017). Because the
129 pseudo-superdiffusion γ parameter depends on the local $\Delta\chi$ at the interface between different tissues
130 and on the distribution and dimension of the diffusion compartments, the γ -metrics could be useful
131 for extracting information complementary to that of the DTI in normal aging studies of the human
132 brain.

133 Starting from the representation of the diffusion weighted (DW) signal in terms of fractional
134 derivatives (Lin, 2015; Lin 2016; Lin 2018), we quantified the γ parameters using the signal, $S(b)$,
135 obtained with a pulse field gradient (PFG) sequence collected by changing diffusion gradient (g_{diff})
136 strength at a constant value of the diffusion time Δ . In this framework, DW signal must be fitted to

137 the stretched exponential function: $S(b) = S(0)\exp(-(bD)^\gamma)$ (Magin et al. 2008, De Santis et al.
138 2011, Hall and Barrick 2012, Ingo et al. 2014). In the context of the transient anomalous diffusion
139 theory, based on the Continuous time random walk (CTRW) (Metzler and Klafter 2000), the γ
140 parameter extracted by fitting the above function to DW data, quantifies superdiffusion processes.
141 Clearly, there is no superdiffusion of water in brain tissues, but the signal representation that we use
142 to quantify γ reflects the additional effect of the magnetization phasing and dephasing due to
143 internal gradients (\mathbf{g}_{int}) generated by $\Delta\chi$ at the interface between different tissues. As explained in
144 our previous papers describing in vitro and ex vivo experiments to validate the γ -metrics (Palombo
145 et al. 2011; Palombo et al 2012; Capuani et al. 2013), an ensemble of spins in a voxel can contribute
146 to a further decrease in the DW signal attenuation, when \mathbf{g}_{int} and \mathbf{g}_{diff} are in the same order of
147 magnitude; other spins (that can be located in a voxel far from the first ones) can acquire a phase
148 that will help to increase the signal. Due to indistinguishable spins associated with water molecules,
149 this scenario mimics a super-diffusion regime where water molecules seem to perform longer jumps
150 because their signal disappear in one spot, while appearing instantaneously in another spot. For this
151 reason, we named γ the pseudo-superdiffusion parameter of transient anomalous diffusion. The
152 adjective “transient” means that over a sufficiently long time, diffusion asymptotically becomes
153 normal (or Gaussian) showing a finite asymptotic diffusion value (percolation limit). In this paper,
154 the potential of γ -metrics in detecting WM and scGM changes due to aging is shown regardless of
155 the debate concerning the existence of transient anomalous diffusion in brain tissues (Nicholson,
156 2015; Saxton, 2008; Destainville et al., 2008), as this issue is outside the scope of this study.
157 Towards this goal, γ -metric results in WM and scGM were compared to DTI parameters, mean
158 kurtosis (MK) derived from DKI metrics (Jensen et al. 2010) and NODDI derived parameters
159 (Zhang et al., 2012). Association between diffusion metrics and subjects’ age was assessed *via*
160 linear regression. We tested the hypothesis whereby γ -metrics are sensitive to physiological and
161 structural variations that occur in the human brain during aging, such as iron deposition and myelin
162 degradation.

163

164 **2 Materials and Methods**

165 **2.1 Studied population**

166 A total of 35 volunteers took part in this study after providing informed written consent in
167 compliance with the national laws and with the local ethics committee guidelines. None in the
168 cohort had a history of stroke, head injuries, medical illness or diagnosis of neurological and
169 psychiatric disorders. Of the 35 volunteers, 32 were retained for this study, 19 men and 13 women
170 (age range 20-77 years, Mean \pm -SD = 43.7 \pm -18.2y). One of the volunteers was excluded due to the

171 presence of brain abnormalities. The other two subjects were discarded because of incomplete data
172 acquisitions and substantial bulk motion.

173 **2.2 Data Acquisition**

174 All volunteers underwent MRI examination using a 3.0T Siemens Magnetom Allegra (Siemens
175 Medical Solutions, Erlangen, Germany) equipped with a circularly polarized transmit-receive coil.
176 The maximum gradient strength was 40 mT/m with a maximum slew rate of 400 T/m/s. The same
177 MRI protocol was applied to all subjects, including whole-brain T1-weighted images and Diffusion-
178 Weighted Spin Echo-Echo Planar Imaging (DW SE-EPI). Care was taken to center each subject's
179 head in the head coil and to restrain subject's motion with cushions and medical tape.

180 Diffusion experiments were performed with the following parameters: $TR/TE = 6400/107$ ms; $\Delta/\delta =$
181 $107/35$ ms; bandwidth = 1860 Hz/px; matrix size = 128×128 , number of axial slices = 32; in-plane
182 resolution = 1.8×1.8 mm²; slice thickness = 3 mm; number of averaged scans NS = 2. The
183 diffusion-encoding gradients were applied along 15 non-collinear directions spanning the entire
184 sphere to minimize the effect of cross-terms between the diffusion gradients and the imaging
185 gradients in the estimation of diffusion parameters (Kingsley, 2006). The set of 15 diffusion
186 directions was chosen among the optimized schemes suggested by Landman et al. being one of the
187 possible minimum potential energy partitions of the scheme of 30 directions proposed by Jones et
188 al., based on the electrostatic repulsion algorithm (Landman et al., 2007, Jones et al., 1999). By
189 varying the gradient strength \mathbf{g} , 11 different b-values were acquired (b = 200, 400, 600, 800, 1000,
190 1500, 2000, 2500, 3000, 4000, 5000 s/mm²), plus the b0 image with no diffusion weighting, with an
191 anterior-posterior phase encoding direction for all the scans. The acquisition time for the entire
192 diffusion protocol was approximately 37 minutes per subject.

193 **2.3 Data analysis**

194 Figure 1 illustrates the main steps of the image processing pipeline used in this study. After the raw
195 data quality check, all diffusion images were pre-processed to correct for noise effects, Gibbs
196 ringing artifacts, eddy currents and subject's movements. DTI, DKI, NODDI and γ -imaging
197 representative functions (see paragraph 2.4) were fitted to different subsets of the diffusion data. A
198 population-based template was constructed, and all images were co-registered to this template. The
199 analysis was finally carried out using both a ROI-based and a voxel-wise based approach.

200 **2.3.1 Pre-processing**

201 All diffusion images were first visually inspected to check for data quality. Datasets with
202 considerable bulk motion artifacts were discarded.

203 To reduce the noise effect on the diffusion parameter estimation, the MRtrix3 *dwidenoise* tool
204 (Copyright © 2016 New York University, University of Antwerp,

205 <https://github.com/MRtrix3/mrtrix3>) was applied as the first step of the preprocessing (Tournier et
206 al., 2012, Veraart et al., 2016a, Veraart et al., 2016b). Then, the Gibbs ringing correction framework
207 of *Kellner et al* (Kellner et al., 2016) was applied for EPI distortion correction. Finally, the image
208 distortions induced by head motion and eddy currents were corrected using the FSL eddy tool
209 (FMRIB Software Library v5.0, FMRIB, Oxford, UK) (Yamada et al., 2014, Andersson and
210 Sotiropoulos, 2016).
211

Volunteers: 32 subjects (Age range 20-77y Mean/SD = 44/18y)

Acquisition scheme: 11 b-shells with 15 directions each + b_0

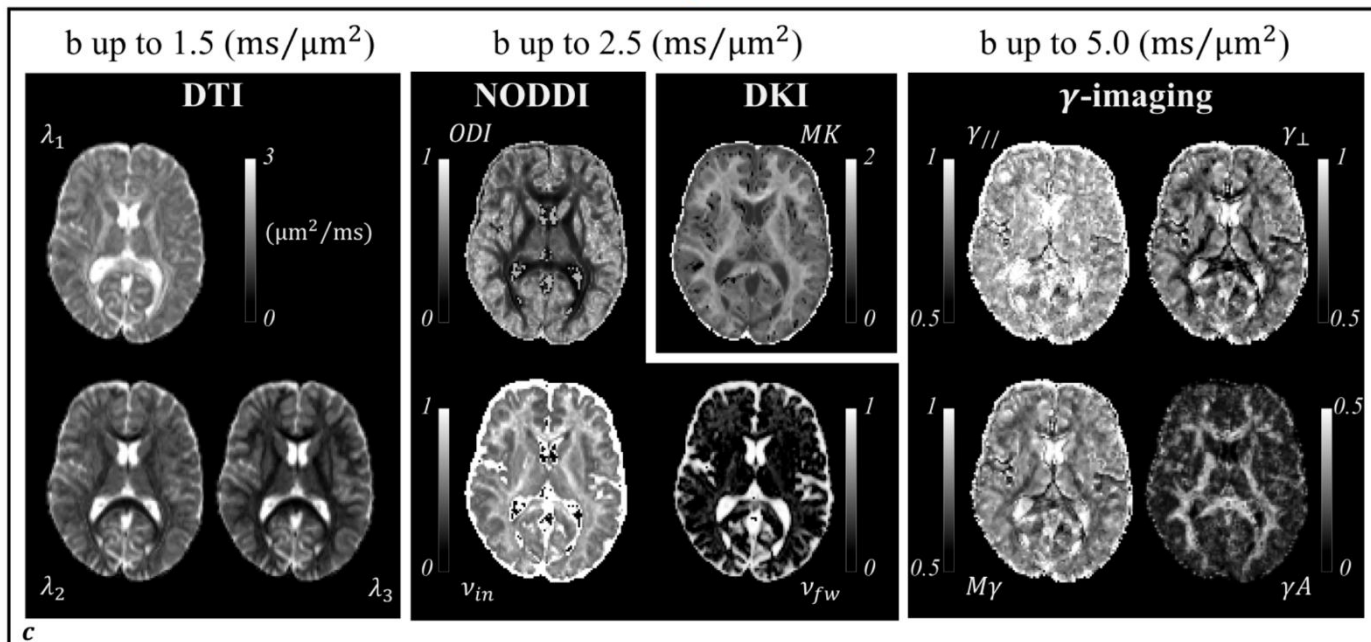
a

Noise correction (*Dwidenoise-MRtrix3*)

Gibbs ringing correction (Kellner *et al.*)

Eddy current correction (*EDDY-FSL*)

b



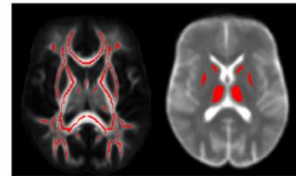
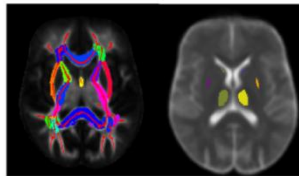
Spatial normalization (*DTI-TK*) + mean FA skeleton (*TBSS*)

Normalization and projection of the other parametric maps

ROI-based analysis

Voxel-wise analysis

d



212

213

214 **Figure 1:** Pipeline of the data processing: the main steps carried out to analyze the diffusion
 215 weighted images are schematically summarized. *a)* Brief description of the subjects' cohort and
 216 acquisition protocol. *b)* The collected data were then corrected for random noise effects, Gibbs
 217 ringing artifacts, movements and eddy current induced artifacts. *c)* Different subsets of the data
 218 were used to obtain the different diffusion metrics. *d)* The DT-eigenvalues were used to obtain a
 219 population specific template; all the other metrics were then projected onto this template.
 220 Associations between subjects' age and diffusion metrics were assessed averaging over regions of
 221 interest (ROIs) or voxel-wise.

222 2.4 Diffusion metrics generation

223 Different subsets of the pre-processed data were used to compute DTI, DKI, NOODI and γ -imaging
 224 diffusion metrics.

225 2.4.1 DTI and DKI

226 The cumulant expansion of the log-transformed diffusion weighted signal in powers of b is the most
 227 widespread signal representation. By truncating the expansion at the second order in b , the following
 228 expression in tensorial form can be obtained (Basser et al., 1994, Jensen et al. 2005):

$$229 \quad \ln \frac{S(b, \mathbf{g})}{S_0} = -\mathbf{b} \sum_{i,j=1}^3 \mathbf{g}_i \mathbf{g}_j \mathbf{D}_{ij} + \frac{1}{6} \mathbf{b}^2 \left(\sum_{i=1}^3 \frac{D_{ii}}{3} \right) \sum_{i,j,k,l=1}^3 \mathbf{g}_i \mathbf{g}_j \mathbf{g}_l \mathbf{g}_k \mathbf{W}_{ijkl} \quad (1)$$

230 Here \mathbf{g} is the direction of the applied diffusion weighting, \mathbf{D} is the rank-2 diffusion tensor and \mathbf{W} is
 231 the rank-3 kurtosis tensor. For moderate b -values, the above expression can be truncated at the first
 232 order, recovering the conventional diffusion tensor imaging (DTI) (Basser et al., 1994).

233 In this study, DTI analysis was performed *via* FSL dtifit tool, considering the b -shells between $b =$
 234 200 and $b = 1500$ s/mm² (i.e. 6 b -values). The dtifit routine returns MD and FA maps together with
 235 the three diffusion tensor eigenvalues ($\lambda_1, \lambda_2, \lambda_3$, with $\lambda_1 > \lambda_2 > \lambda_3$) and eigenvectors (V_1, V_2, V_3),
 236 which define the DTI reference frame (DTI-rf) voxel-wise. The axial ($D_{//}$) and radial (D_{\perp}),
 237 diffusivities were computed as follows: $D_{//} = \lambda_1$, $D_{\perp} = (\lambda_2 + \lambda_3)/2$.

238

239 By fitting equation (1) to the logarithm of the signal, having acquired at least 21 measures
 240 distributed over two b -shells, it is possible to reconstruct the kurtosis tensor \mathbf{W} (Jensen et al. 2005).
 241 Diffusion kurtosis imaging (DKI) is a clinically feasible extension of DTI at higher b -values that
 242 probes restricted water diffusion in tissues providing information about the tissue complexity.

243 In this work, we used the b -shells up to the $b = 2500$ s/mm² to get mean kurtosis (MK) weighted
 244 maps. In order to obtain these maps we used the `dki_lls` method from the `md-dmri` software
 245 (<https://github.com/markus-nilsson/md-dmri/tree/master/methods>). After obtaining the \mathbf{W} tensor
 246 components, MK was calculated voxel-wise as the average of \mathbf{W} elements across the sphere, in a
 247 fast and robust way (Hansen et al., 2013).

248

249 **2.4.2 NODDI**

250 The NODDI model function (Zhang et al., 2012) was fitted to all the b-shells up to $b = 2500 \text{ s/mm}^2$,
251 using the toolbox available online (https://www.nitrc.org/projects/noddi_toolbox). NODDI is a
252 biophysical tissue model for DW data that aims to infer specific information about the tissue micro-
253 structure. The normalized total diffusion signal, A , is expressed as the sum of contributions from
254 different compartments:

$$255 \quad A = (1 - v_{fw})[(1 - v_{in})A_{en} + v_{in}A_{in}] + v_{fw}A_{fw}, \quad (2)$$

256 where A_{in} and v_{in} represent the intra-neurite normalized signal and volume fraction, A_{en} is the extra-
257 neurite normalized signal and A_{fw} and v_{fw} represent the normalized signal and volume fraction of the
258 compartment modeling isotropic free-water contributions to the signal (such as CSF). Fitting
259 NODDI to DW-data makes it possible to obtain an estimate of v_{in} and v_{fw} , with values comprised
260 between 0 and 1. Moreover, NODDI quantifies the so-called orientation dispersion index (ODI) that
261 attempts to estimate the orientation dispersion of the neurites within each voxel. ODI values run
262 from 0, referring to an isotropically oriented distribution, to 1, referring to a perfectly coherent
263 bundle of fibers.

264

265 **2.4.3 γ -imaging**

266 Several theoretical models have been proposed to describe anomalous diffusion phenomena, such as the
267 (CTRW) model (Metzler and Klafter 2000), the fractional motion (FM) model and others (Metzler et al.
268 2014). The adaptation of these models to MRI diffusion experiments, permits fitting of experimental DW
269 data to functions containing stretched exponentials and others derived parameters (Magin et al. 2008; Zhou
270 et al. 2010; Ingo et al. 2014; Caporale et al. 2017; Yu et al. 2018; Karaman and Zhou 2018). Unfortunately,
271 different authors have assigned different nomenclatures to indicate the same parameter, fueling the
272 confusion that characterizes the literature of anomalous diffusion methods in MRI.

273 Recently, two anomalous diffusion parameters were introduced in NMR: α and γ . α quantifies sub-diffusive
274 processes and it is measured by varying diffusion time Δ in a pulse field gradient (PFG) MRI sequence.
275 Conversely, γ quantifies super-diffusive processes characterized by a divergence of the jump length
276 variance, and it is measured by varying gradient strengths g in a PFG sequence at a fixed value of Δ
277 (Palombo et al. 2011; Capuani et al. 2013). In the present work, diffusion experiments by varying g at a
278 fixed value of Δ were performed. Therefore, super-diffusive processes were quantified. Clearly, no real
279 super-diffusive processes of water in biological tissues exist, but “pseudo-superdiffusion” processes mainly
280 due to a local background gradient derived from $\Delta\chi$ at the interface between different diffusion

281 compartments and to the different diffusion lengths with which the water molecules diffuse in several
 282 compartments.

283 As the diffusion weighted NMR signal is proportional to the Fourier transform (FT) of the motion
 284 propagator (MP), for investigating pseudo-superdiffusive processes it is possible to use the
 285 following function (Metzler and Klafter 2000) as FT of the anomalous diffusion MP:

$$286 \quad W(q, t) \simeq \exp[-K_{2\gamma}|2\pi q|^{2\gamma}\Delta] \quad (3)$$

287
 288 where $K_{2\gamma}$ is a generalized diffusion constant, whose units are $(\text{ms}^{-1})^{2\gamma}$ with $q=1/(2\pi)\Gamma g\delta$ the wave vector
 289 and $0 < \gamma < 1$. For a fixed value of Δ , the stretched exponential form of signal attenuation as a function of b
 290 value can easily be derived from (3). Indeed, by replacing $|2\pi q|^{2\gamma} = b^\gamma/\Delta^\gamma$ in (3), the following relations can
 291 be obtained:

$$292 \quad \frac{S(b)}{S(0)} \simeq \exp\left[\frac{K_{2\gamma}}{\Delta^{(\gamma-1)}} b^\gamma\right] = \exp\left[\frac{D \rho^{2(\gamma-1)}}{\Delta^{(\gamma-1)}} b^\gamma\right] = \exp[-(D_{\text{eff}}b)^\gamma] \quad (4)$$

293
 294 where D is the diffusion coefficient, $\rho^{2(\gamma-1)}$ and $\Delta^{(\gamma-1)}$ are fractional order space and time constants
 295 that preserve units, and D_{eff} is a generalized effective diffusion constant.

296 All the b -shells were used for γ -imaging analysis. To obtain the γ metrics, a custom-made Matlab
 297 script (MATLAB R2016b) was used. Specifically, the approach described by *Caporale et al.*,
 298 (Caporale et al., 2017) was used in which the reference frame of the tensor representing the transient
 299 anomalous diffusion was assumed to coincide with that of the DTI (DTI-rf) (De Santis et al., 2011,
 300 Caporale et al., 2017). The choice of projecting the stretched γ -exponents along the axes of DTI-rf
 301 assumes that, to a first approximation, anomalous and normal (i.e. Gaussian) diffusion share the
 302 same rotationally invariant reference frame (De Santis et al. 2011). The resulting signal
 303 representation showing transient anomalous pseudo-superdiffusion is written as:

$$304 \quad \frac{S(b)_j}{S(0)} = e^{-\sum_{i=1}^3 A_i (b(V_i \cdot g_j))^{\gamma_i}} \quad (5)$$

305
 306 Here j denotes the diffusion direction defined by the gradient vector g_j ; i indicates each of the 3
 307 main axes with respect to a diffusive motion along a generic direction which may be decomposed; γ_i
 308 and A_i are, respectively, the anomalous diffusion exponents and the generalized diffusion
 309 coefficients estimated along the direction identified by the eigenvector V_i in the DTI-rf.

310 The estimated γ -exponents $\gamma_1, \gamma_2, \gamma_3$ (with $\gamma_1 > \gamma_2 > \gamma_3$) are adimensional parameters that take
 311 values from 0 to 1. γ_i equal to 1 indicates a normal Gaussian diffusion, while values of $\gamma_i < 1$

314 indicate a departure from Gaussian diffusion. The following γ -metrics were finally computed:
 315 axial- γ ($\gamma_{//} = \gamma_1$), radial- γ ($\gamma_{\perp} = \frac{\gamma_2 + \gamma_3}{2}$), mean- γ ($M\gamma = \frac{\gamma_1 + \gamma_2 + \gamma_3}{3}$), γ -anisotropy ($\gamma_A =$
 316 $\sqrt{\frac{3[(\gamma_1 - M\gamma)^2 + (\gamma_2 - M\gamma)^2 + (\gamma_3 - M\gamma)^2]}{2(\gamma_1^2 + \gamma_2^2 + \gamma_3^2)}}$). Specifically, $\gamma_{//}$ represented the projection of the anomalous
 317 exponent in the direction described by the first eigenvector \mathbf{V}_1 of the Gaussian diffusion tensor,
 318 whereas γ_{\perp} was derived by an average of the other two orthogonal projections (De Santis et al.,
 319 2011).

320

321

322 2.5 Post-processing

323 2.5.1 Image registration

324 A registration pipeline similar to that proposed by *Timmers et. al* (Timmers et al., 2016) was used. Briefly, a
 325 population-specific template was obtained with DTI-TK software (available on
 326 <http://www.nitrc.org/projects/dtitk>). The algorithm applies a deformable registration to the DTI-derived
 327 eigenvalues and improves the registration outcome compared to analogous algorithms based on FA maps
 328 (Zhang et al., 2006; Keihaninejad et al., 2013, Wang et al., 2011). The resulting normalized images were
 329 used to compute the standard FA , MD , $D_{//}$ and D_{\perp} maps with a higher resolution compared to the original
 330 maps (voxel size = $1 \times 1 \times 1$ mm³).

331 The TBSS tool of FSL (Smith et al., 2006) was used to obtain a mean FA skeleton for the WM
 332 tracts common to all subjects in the normalized space. The threshold limit value of this skeleton was
 333 set to 0.4 in order reduce bias due to cross subject variability of the WM tracts. Finally, the
 334 participant-specific transformation fields, obtained during the tensor-based transformation, were
 335 used to normalize all the other diffusion metrics used in this study as specified by Timmers et al. in
 336 supplementary methods (Timmers et al., 2016).

337

338 2.5.2 ROI based analysis

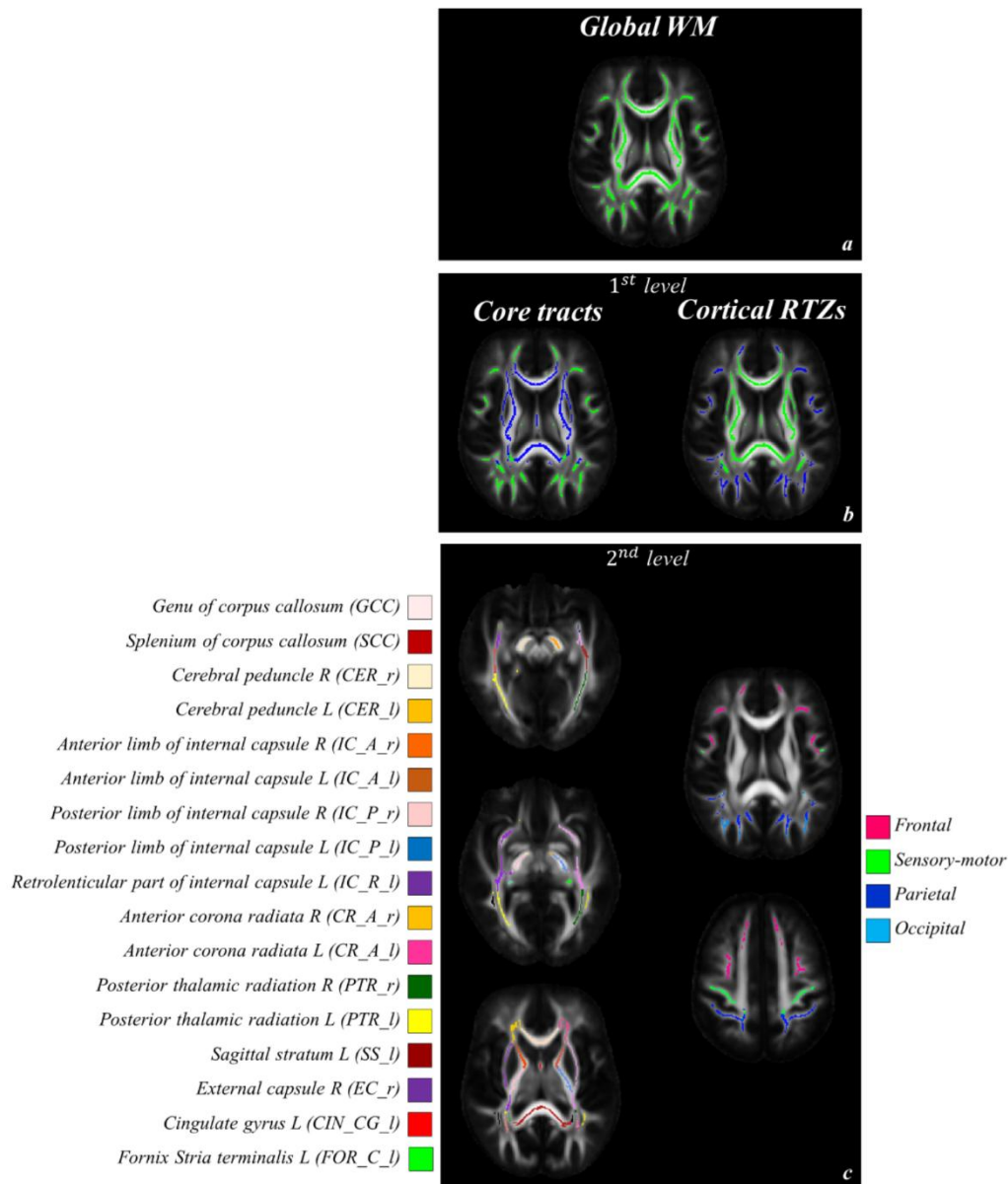
339 Analysis of the correlation between diffusion metrics and subjects' age was performed on a region
 340 of interest (ROI) basis using a hierarchical approach in order to better understand the spatial patterns
 341 of aging (Simmonds et al., 2014, Chang et al., 2015). The age-related modifications were calculated
 342 separately for WM ROIs and sub-cortical GM (scGM) ROIs.

343 As regards WM, the global trajectories were first obtained averaging the different metrics along
 344 all the voxels belonging to the WM skeleton. Subsequently, two groups of WM regions were
 345 selected. Following the nomenclature proposed by Simmonds *et al.*, the “core tracts” were selected
 346 as the intersection of the WM skeleton and the JHU-DTI81 atlas (Mori et al., 2008). The “cortical

347 regional termination zones” (RTZs) were defined as the intersection of the cortical GM regions
348 derived from the Harvard-Oxford (HO) atlas in FSL and the WM skeleton. The two groups of WM
349 tracts were further partitioned in sub-tracts. The core tracts were divided using the JHU’s own
350 parcellation (http://www.loni.usc.edu/ICBM/Downloads/Downloads_DTI-81.shtml). The cortical
351 RTZs were divided into frontal, sensory-motor, parietal and occipital tracts. All the above steps are
352 summarized in Figure 2.

353 Regarding the scGM ROI analysis, the HO subcortical atlas was used to identify the different
354 structures. To avoid partial volume effects each element from the atlas was eroded via the “-ero”
355 routine of `fslmaths` in FSL, using a spherical filter with a 2 mm radius. Because of the limited field
356 of view in the axial direction, only the inner structures of the subcortical GM were retained for the
357 analysis. The caudate, the thalamus, the putamen and the pallidum were considered in the study. In
358 addition, a global trajectory was obtained from the average of all voxels belonging to the examined
359 regions.

360 The average of each diffusion metrics was then calculated for each ROI. The association between
361 the resulting values and the subjects’ age was assessed *via* linear regression using the free software
362 R (R Core Team 2013 <http://www.R-project.org/>). Also, the shared variance between any two
363 metrics was assessed for the global trajectories. Correlation was considered statistically significant
364 when the derived p-value was ≤ 0.05 after correcting for family-wise error ($p_{fwe} \leq 0.05$), *i.e.*
365 multiplying p by the number of regions considered in the group under analysis.
366 p-value ≤ 0.05 without controlling for family-wise error ($p \leq 0.05$) were also reported for
367 comparison with relevant regions highlighted in previous studies (Billet et al. 2015, Kodiweera et
368 al. 2016).



369

370

371 **Figure 2:** WM atlas description to illustrate the multi-level ROI-based approach used to analyze and
 372 display the results. *a)* the global WM atlas is defined by the skeleton obtained with the skeletonize
 373 command of FSL using a threshold of 0.4. *b)* In the first level of the subdivision the core tracts are
 374 obtained from the intersection between the WM skeleton, the JHU atlas, while the cortical regional
 375 termination zones (RTZs) are obtained from the intersection between the WM skeleton and the
 376 Harvard-Oxford cortical atlas. *c)* In the second level of the subdivision, the core tracts and cortical
 377 RTZs are further divided into sub-regions according to the atlas nomenclatures; 29 sub-regions for
 378 the core tracts and 4 for the cortical RTZs were identified. Only those regions are reported that share
 379 at least one association between diffusion metrics and aging.
 380

381 2.5.3 Voxel-wise analysis

382 To test the effect of aging on the diffusion metrics voxel-wise, permutation-based statistics was
 383 carried out on both the WM and scGM. All diffusion metric maps were performed with the WM

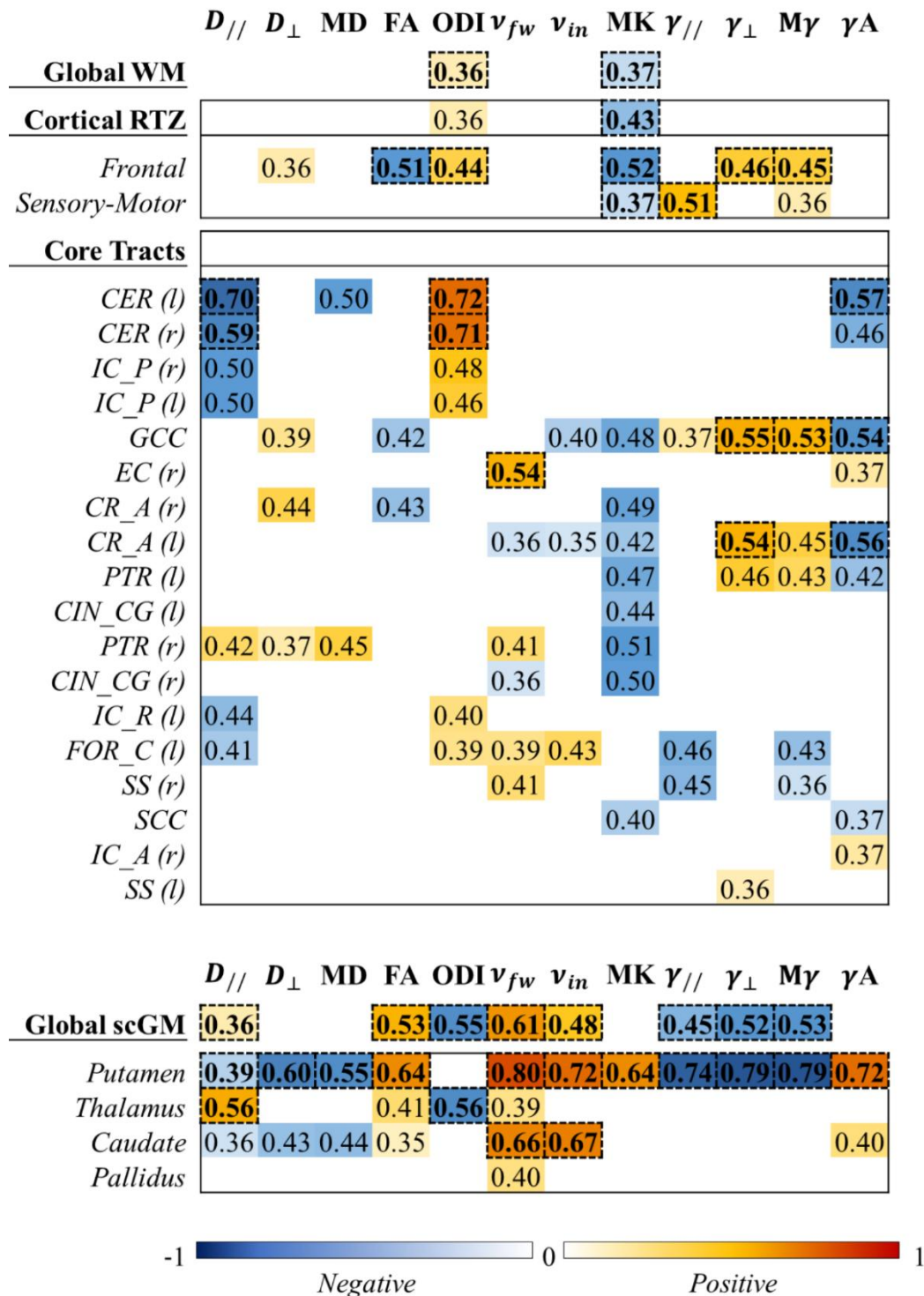
384 skeleton and the scGM eroded mask, respectively. FSL's randomize command was used with 5000
385 permutations to generate the statistic maps. The Threshold-Free Cluster Enhancement (TFCE)
386 option was used to correct p-values for family wise errors ($p_{fwe} \leq 0.05$).

387

388 **3 Results**

389 **3.1 ROI analysis**

390 To display the results, we used a figure format like the one used by Billet et al. (Billet et al., 2015).
391 For each ROI and each diffusion metrics we reported the correlation coefficient when $p < 0.05$.
392 Red-yellow colors stand for positive correlation, while blue-cyan colors stand for negative
393 correlation. The regions, where a linear correlation with a family-wise error corrected p-value was
394 found significant ($p_{fwe} < 0.05$), are highlighted in bold and by boxes with dashed contours. Figure 3
395 shows the results for WM ROIs (at the top) and scGM (at the bottom), whereas Figure 4 shows plots
396 of different diffusion metrics vs subjects' age in different regions of WM and scGM.



397

398 **Figure 3:** ROI-based results obtained using the multi-level ROI-based analysis in white matter
 399 (WM), at the top, and subcortical gray matter (scGM), at the bottom. The colored cells indicate the
 400 regions where a correlation between a diffusion parameter and age was found ($p < 0.05$). Warm
 401 colors indicate positive correlation, while cold colors indicate negative correlation. Regions
 402 showing a significant correlation after correction for family-wise errors are highlighted in bold and
 403 by boxes with dashed contours.

404

405

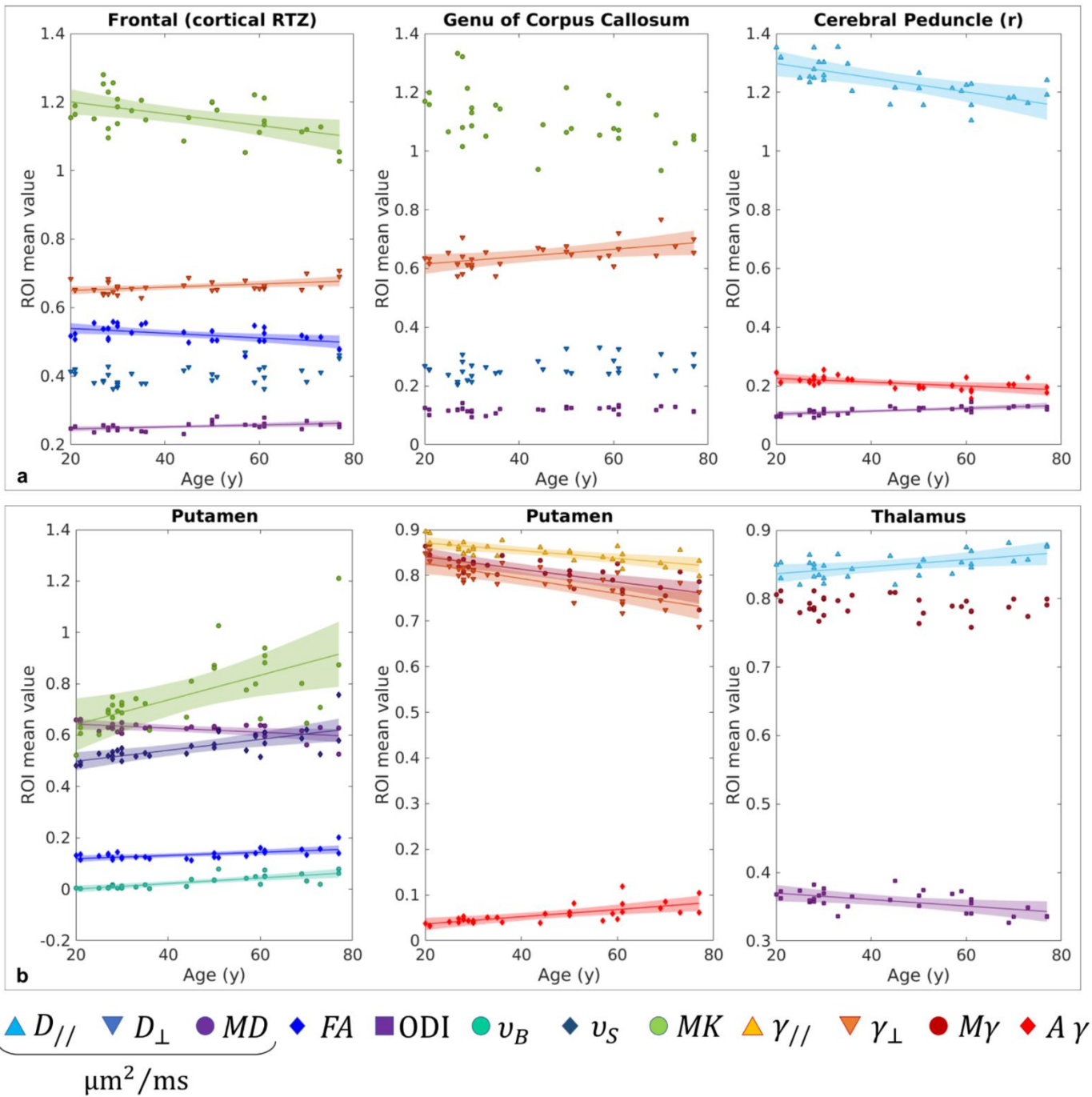
406 3.1.1 Results in WM

407

408 $D_{//}$ and FA are the only parameters of DTI metrics that show significant correlation with aging,
409 exhibiting mostly a negative association. $D_{//}$ tends to decrease with aging in the cerebral peduncle
410 (CER), while FA presents a decrease in frontal WM. Regarding the parameters obtained using
411 higher b-shells, MK shows a negative association, while ODI and v_{fw} of NODDI positively
412 correlate with aging. v_{in} shows weak negative trends within the genu of corpus callosum (GCC) and
413 the left anterior corona radiata (CR_A (l)) but a positive trend in the left fornix stria terminalis
414 (FOR_C (l)).

415 All γ metrics show at least one significant correlation. $\gamma_{//}$, γ_{\perp} and $M\gamma$ generally increase although $\gamma_{//}$
416 and $M\gamma$ show a decrease in the left retrolenticular part of the internal capsule (IC_R (l)) and right
417 sagittal striatum (SS (r)). On the other hand, γ_A generally decreases with advancing age (see Figures
418 3 and 4).

419 As regard the global WM atlas, ODI and MK were the only parameters showing a significant trend.
420 The MK decrease seemed to be driven by a decrease within the cortical RTZs rather than in the core
421 tracts. In particular, the tracts close to the frontal lobe showed the greatest number of significant
422 differences. FA and MK decreased while ODI , γ_{\perp} and $M\gamma$ increased. MK decreased also in the tracts
423 close to the sensory-motor lobe along with a parallel increase in $\gamma_{//}$. No general trends related to core
424 tracts were observed, however several region-specific trends were recognized within the
425 parcellation. On average, the regions showing the strongest correlation were the left and right sides
426 of the CER. Here, a simultaneous decrease in $D_{//}$ and increase in ODI were observed. Also, a
427 significantly decreased anisotropy in γ was observed. The same pattern of decreased axial diffusivity
428 and increased ODI applied also to both sides of the internal capsule (IC_P), although not statistically
429 significant. γ -derived parameters showed a rather strong correlation within the GCC and (CR_A (l)).
430 Among these metrics, γ_{\perp} seemed to be the driving one inducing an increase in $M\gamma$ and a decrease in
431 γ_A . A positive association was found in the left external capsule between v_{fw} and age. As regards
432 MK , several negative trends were observed within the core tracts, but none of them were strong
433 enough to be considered significant.



434

435

436 **Figure 4:** Plots of different diffusion metrics vs age in different regions of WM and scGM. Box *a*
 437 shows the trends in WM: the frontal part of the cortical RTZs, the left cerebral peduncle (CER (*l*))
 438 and the genu of corpus callosum (GCC) are reported. Box *b* shows the trends in scGM. The trends
 439 within the putamen and the thalamus are reported. On the top-right panel the markers and colors
 440 identifying the different parameters. Solid lines are reported where a statistical significance was
 441 found ($p_{fwe} < 0.05$.) The shaded area represents the confidence interval of 95%.

442 3.1.2 Results in subcortical GM

443 Besides a few cases, a complete inversion of age-related trends was observed for all the parameters
 444 in the sub-cortical regions (Figure 3): D_{\perp} , MD , ODI , $\gamma_{//}$, γ_{\perp} and $M\gamma$ showed a decrease, whereas FA ,

445 v_{in} , v_{fw} , γA showed an increase with age. $D_{//}$ showed a positive and negative association with age in
446 the thalamus and in the putamen, respectively. The putamen was with no doubt the region showing
447 the most widespread and strongest correlation with diffusion derived parameters (*i.e.* all apart from
448 ODI). The thalamus showed a pattern similar to that of the CER, but inverted, *i.e.* increased $D_{//}$ and
449 decreased ODI. Finally, the caudate showed a parallel increase in v_{in} and v_{fw} with aging.

450 3.2 Voxel-wise analysis

451 The results of the voxel-wise approach were coherent with those found using the ROI-based
452 approach. Regional differences in WM are displayed in Figure 5. $D_{//}$ and ODI showed mono-lateral
453 differences in the left cerebral peduncle and in the left posterior limb of the internal capsule. This
454 result may highlight a possible associated variation of $D_{//}$ and ODI (Billiet et al. 2015). A general
455 increase in $M\gamma$ and γ_{\perp} vs age was also highlighted (Figure 5). The effects are widespread in the left
456 frontal area, including the left corona radiata and part of the genu of corpus callosum. In accordance
457 with the results found in the ROI-based analysis, v_{in} showed a significant increase within the right
458 external capsule. No significant association between MK and age was found in the WM voxel-wise
459 analysis.

460 Figure 6 shows the trends of the conventional DTI-parameters and NODDI-parameters in scGM. In
461 the putamen, a decrease in MD together with an increase in FA, v_{in} and v_{fw} were observed. v_{in}
462 increased also in the caudate, while an increase in v_{fw} was observed in the posterior part of the
463 thalamus. ODI decreased in the thalamus with a spotty pattern. The voxel-wise correlations of γ -
464 derived metrics vs age in scGM are highlighted in Figure 7. The strong increase in $M\gamma$ and decrease
465 in γA seemed to be driven by a variation in γ_{\perp} , rather than $\gamma_{//}$.

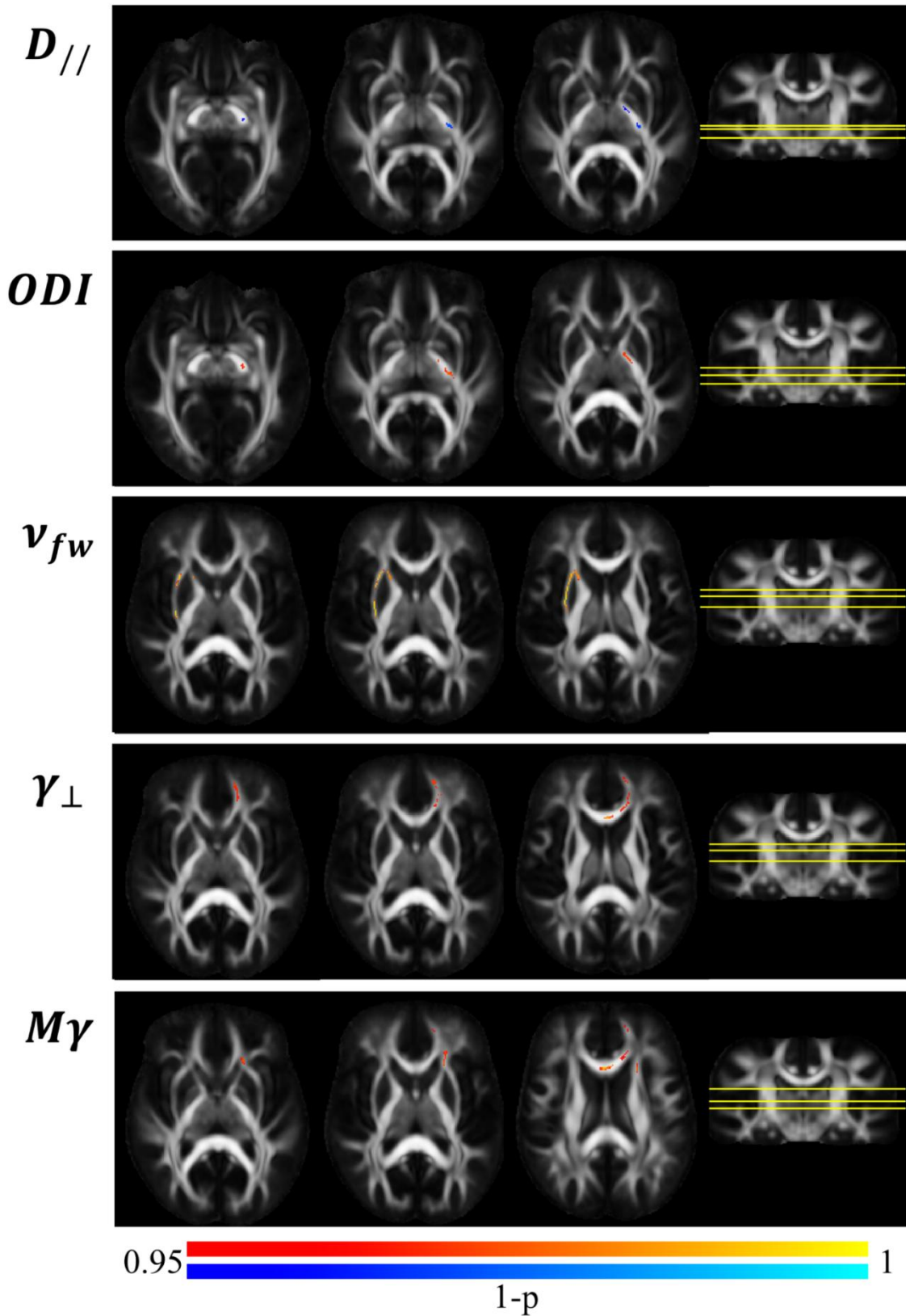
466

467 3.3 Correlation between metrics

468 The squared values of linear cross-correlation coefficients calculated between metrics both in total
469 WM and total scGM are displayed in Figure 8. These values represent the amount of variance that
470 each metrics shares with the others, giving an estimate of how unique the information provided by
471 each metrics is. As expected, the variance shared by parameters derived from the same metrics is
472 high. In WM, D_{\perp} seems to account for most of the variability of FA and MD. v_{in} shares a large
473 portion of variance with all the DTI parameters and specifically with MD and D_{\perp} , while ODI has a
474 negative association with $D_{//}$. MK shares a rather high portion of variance with MD, FA, and D_{\perp} . γ -
475 derived parameters have a rather small portion of variance shared with the other diffusion metrics.
476 The only exception is $\gamma_{//}$ that shows a stronger association with MD, FA and MK.

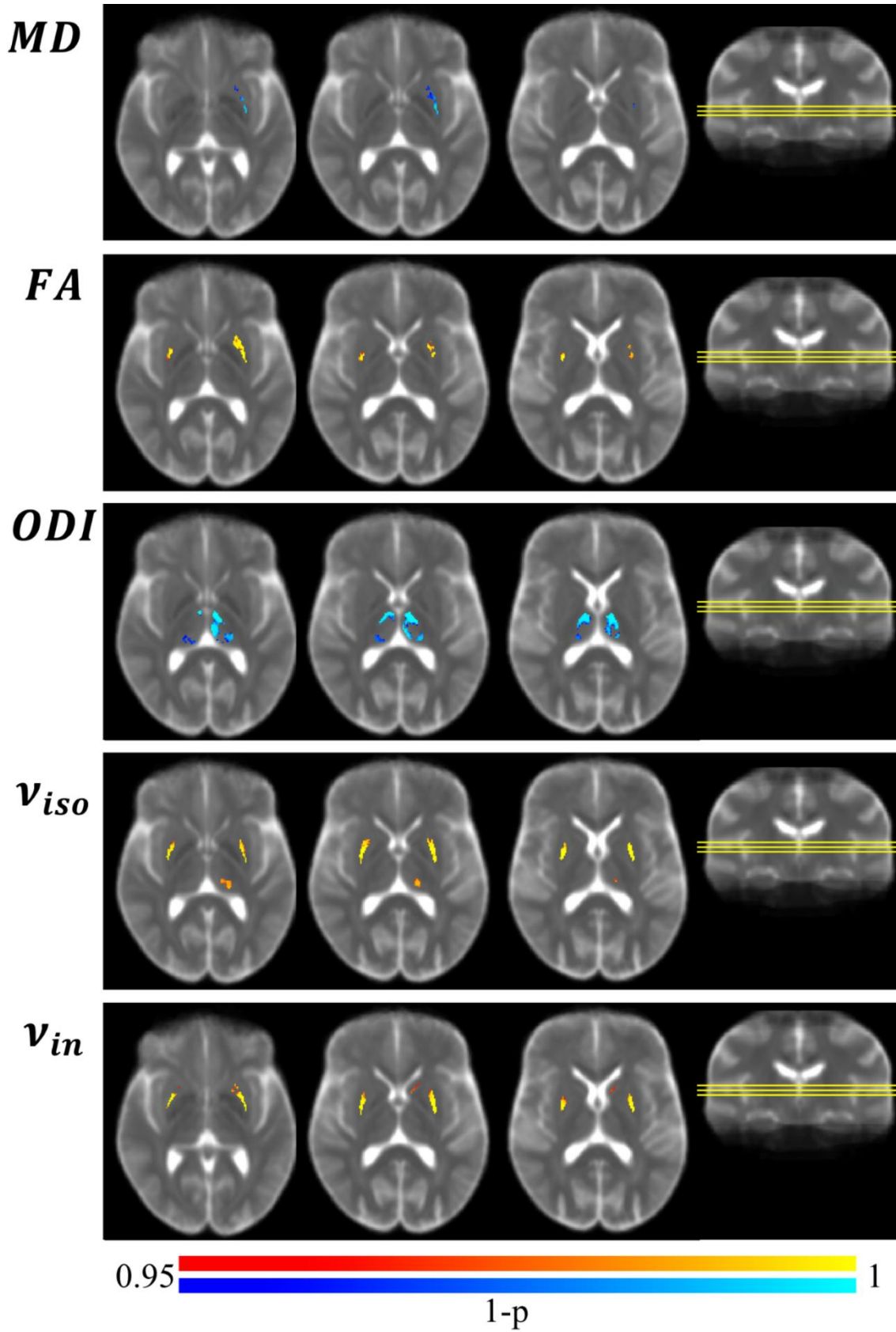
477 The right side of Figure 8 shows the results for scGM. The results appear to be clustered in a
478 different way. MD and FA on the one hand and $M\gamma$ and γA on the other, share a large proportion of

479 variance with D_{\perp} and γ_{\perp} , respectively. ODI measure shows a negative correlation only with $D_{//}$ and
 480 FA. All the metrics obtained using higher b-shell seem to share a larger portion of variance. In
 481 particular, v_{in} and v_{fw} show a much higher association with γ -metrics, compared to that shown in
 482 WM.



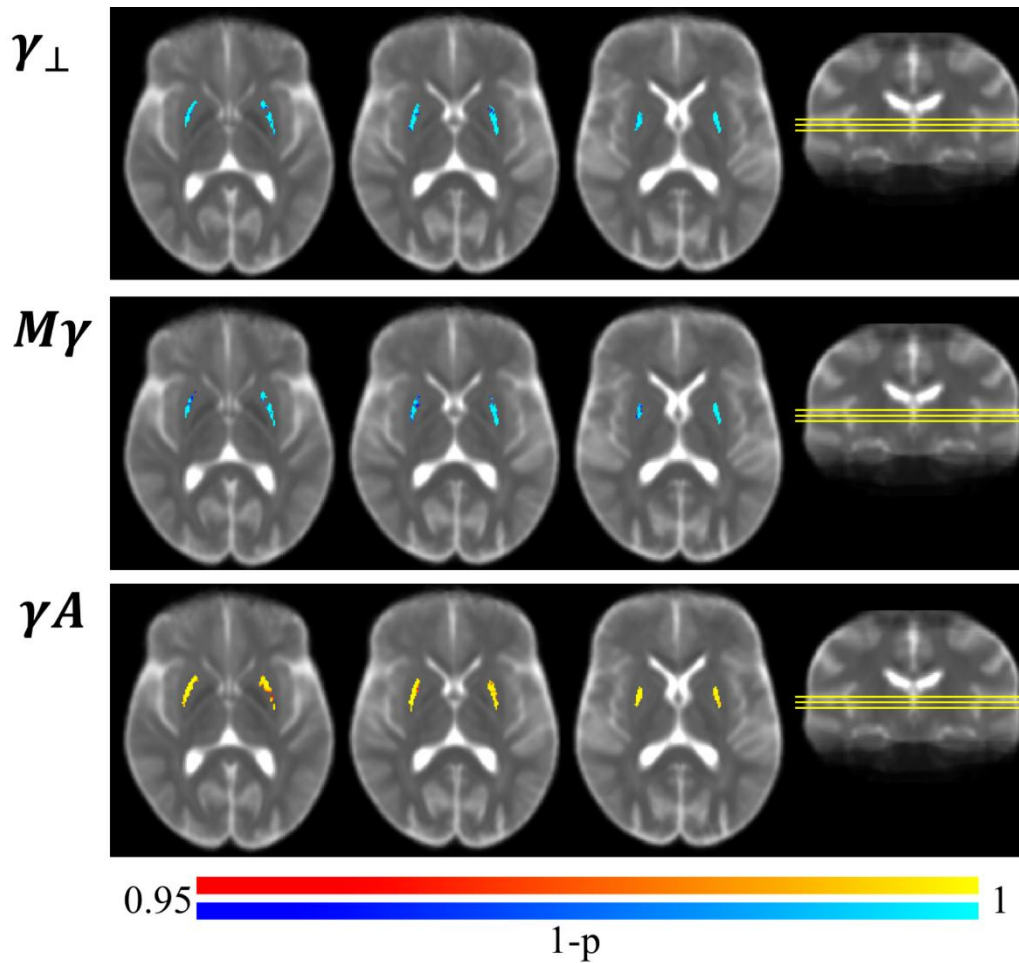
483

484 **Figure 5:** Results of the voxel-wise analysis of DTI-, NODDI- and γ -metrics correlation with
485 subjects' age in WM. The maps show the corrected p-value ($1 - p$) superimposed on the population
486 specific *FA* template. The red-yellow colors denote positive correlation, while the blue-cyan colors
487 denote negative correlation.



488

489 **Figure 6:** Results of the voxel-wise analysis of correlation between DTI- and NODDI-derived
 490 parameters and subjects' age in scGM. Here the results are superimposed on *MD* population specific
 491 template. The red-yellow colors denote a positive correlation, while the blue-cyan colors denote a
 492 negative correlation.



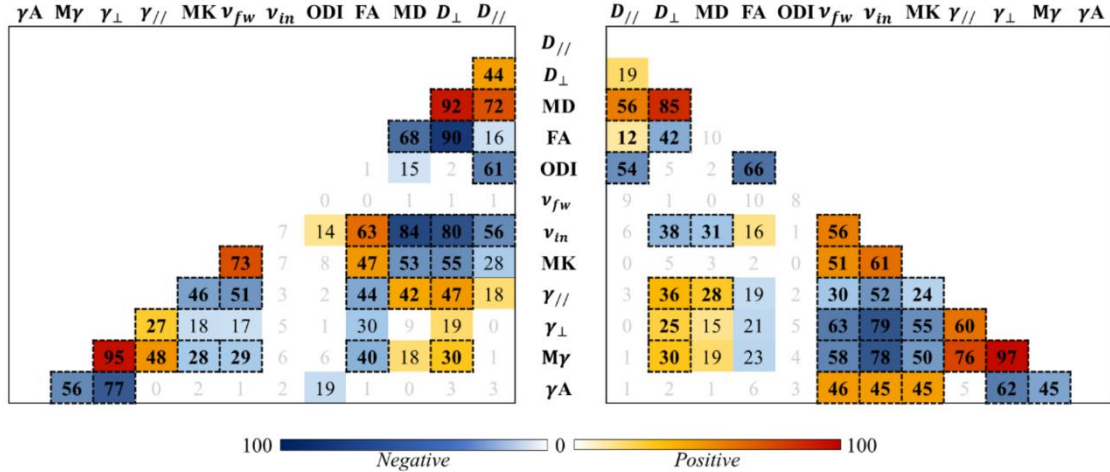
493

494 **Figure 7:** Results of the voxel-wise analysis of correlation between γ -metrics and subjects' age in
 495 scGM. The results are superimposed on *MD* population template. The red-yellow colors denote a
 496 positive correlation, while the blue-cyan colors denote a negative correlation.

497

498

499



500

501 **Figure 8:** The shared variance between diffusion metrics is displayed separately for white matter
 502 (WM), on the left, and subcortical gray matter (scGM), on the right. The higher the reported value,
 503 the higher the similarity of the information provided by the two metrics. Warm colors show positive
 504 correlation, cold colors represent negative correlation. Significant correlation, corrected for family-
 505 wise errors, are highlighted in bold and by a box with dashed contours.

506

507 4 Discussion

508 In this cross-sectional study we assessed the potential of a combined use of γ -metrics and other more
 509 widespread diffusion MRI (dMRI) techniques in detecting the microstructural and physiological
 510 changes due to normal aging in WM and scGM of the human brain. Previous works (Caporale et al.
 511 2017) highlighted how γ -metrics may reflect inhomogeneities due to $\Delta\chi$ among various tissues and
 512 compartments, being potentially useful as an indirect measure of myelin integrity and iron content.
 513 In this paper, the cohort of volunteers spanned from young adults to elderly subjects. To analyze the
 514 different regions of the brain, we used a hierarchical ROI-based approach in parallel with a voxel-
 515 wise-based approach, both in WM and scGM. We found diversified patterns of parameter
 516 modifications with advancing age, both in scGM and WM, possibly indicating regional-specific
 517 aging processes. The results suggest that γ -metrics is complementary to DTI, DKI and NODDI,
 518 highlighting changes not significantly detected by the other conventional metrics.

519

520 4.1 Microstructural changes in white matter

521 The results of this study suggest that a combination of different dMRI-derived techniques permits
 522 observation of microscopically different aging patterns within the WM fibers.

523 The aging of WM fibers appears to be driven by two principal mechanisms: the degradation of
 524 nerve fibers and the degeneracy of the myelin (Peters, 2009, Peters and Kemper, 2012). On one

525 hand, degenerating nerve fibers start to accumulate mixtures of organelles and neurofilaments.
526 These accumulations are often related to dystrophy of the axons such as swelling. The degeneration
527 process ends with the complete disintegration of the axon. The extent of lost fibers, in some specific
528 regions of rhesus monkeys' brains, has been quantified to be around 20% in the genu of corpus
529 callosum, 30% in the splenium of corpus callosum and 45% in the anterior commissure (Sandell and
530 Peters, 2003, Bowley et al., 2010). On the other hand, myelin undergoes segmental demyelination
531 that is often followed by remyelination and sometimes by myelin decompaction. Remyelinated
532 segments are thinner and shorter, while decompaction is principally caused by splitting of myelin in
533 the major dense line (Peters, 2009, Peters and Kemper, 2012, Sandell and Peters, 2003, Bowley et
534 al., 2010).

535 dMRI has been extensively used with the aim to track these microscopic changes in vivo. A large
536 number of cross-sectional studies (Pfefferbaum et al., 2000, Abe et al., 2002, Salat et al., 2005,
537 Sullivan et al., 2010, Ardekani et al., 2007, Giorgio et al., 2010), but also longitudinal studies
538 (Barrick et al., 2010) reported an increase in MD and a decrease in FA. Specifically, FA
539 modifications seem to be mostly related to grater D_{\perp} rather than D_{\parallel} (Zhang et al., 2010, Bartzokis et
540 al., 2012), suggesting that the FA reductions are linked to myelin degradation and axonal loss.
541 However, some authors pointed out that care should be taken when interpreting these results
542 (Wheeler-Kingshott and Cercignani, 2009).

543 MK has been shown to decrease with aging (Lätt et al., 2013, Gong et al., 2014, Coutu et al., 2014)
544 indicating a less complex organization of tissues in elderly brains. However, Billet et al. (Billet et
545 al., 2015) reported contrasting results showing an increased MK with ageing. However, the
546 investigated age-range was narrower compared to the population studied by the above-mentioned
547 authors.

548 Few studies reported the association between NODDI parameters and aging (Billet et al., 2015,
549 Cox et al., 2016). v_{fw} was observed to decrease in both studies, while contradictory results were
550 reported for v_{in} and ODI: Billet et al. reported an increase in both these parameters, while Cox et al.
551 reported a decrease in both cases. However, the two studies dealt with different age ranges. In a
552 study carried out on a cohort of young to middle-aged adults, Kodiweera et al (Kodiweera et al.,
553 2017) reported an increase in ODI with aging and observed how this parameter was the most
554 sensitive to microstructural changes compared to DTI parameters.

555 In order to explain the overall trends of age-related microscopic changes, several neurodegenerative
556 theories have been proposed in the past years. For example, it has been established that age-related

557 modifications occur with frontal predominance (Abe et al., 2002, Salat et al., 2005, Ardekani et al.,
558 2007, Sullivan et al., 2010), thus an anterior-posterior gradient of degeneration has been proposed
559 (Pfefferbaum and Sullivan, 2006). On the other hand, according to the retrogenesis theory,
560 demyelination is the major driving mechanism of degeneration and the late myelinating fibers are
561 more affected than the early myelinating ones (Stricker et al., 2009, Cox et al., 2016). Finally, the
562 Wallerian degeneration theory proposes that axonal degradation is the result of injuries happening
563 further from the degradation site (Damoiseaux et al., 2009, Davis et al., 2009).

564

565

566

567 **4.1.1 Is γ -imaging sensitive to myelin degradation?**

568 In the past years, *in vitro*, *ex vivo* and *in vivo* experiments were performed to investigate the features
569 of the so called pseudo-superdiffusion γ parameter (Palombo et al. 2011; Palombo et al. 2012;
570 Capuani et al. 2013; Caporale et al. 2017). The experiments coherently showed that γ quantifies
571 water molecules diffusing with a wide distribution of diffusion lengths in heterogeneous and multi-
572 scale tissues. The width of this set of diffusion lengths is partially due to water diffusion
573 compartmentalization, but also to the inhomogeneity (or averaged internal gradients g_{int}) coming
574 from local $\Delta\chi$ between compartments. In the human brain, $\Delta\chi$ arises from differences in non-heme
575 iron contents and iron-storage proteins and from various degrees of myelin density and orientation
576 with respect to B_0 . It has been found that γ values decreased in parallel to $\Delta\chi$ -derived g_{int} increase
577 (Palombo et al. 2011; Palombo et al. 2012; Capuani et al. 2013; Caporale et al. 2017). Moreover, by
578 repeating the γ -imaging studies in the brain of distinct groups of healthy subjects, using acquisitions
579 obtained with a different number of diffusion gradient directions, we found an excellent agreement
580 between the mean γ values representative of certain brain regions (De Santis et al. 2011;
581 GadElkarim et al. 2013; Caporale et al. 2017).

582 Our results show a significant increase in γ_{\perp} as a function of age in frontal WM and more
583 specifically in the genu of corpus callosum and anterior corona radiata (figures 3, 5). We suggest
584 that these results which are in agreement with our previous findings (Caporale et al. 2017), may
585 reflect an effective decrease in the thickness and integrity of the myelin sheaths across the densely
586 packed WM fibers. Indeed a reduction of myelin would affect the g_{int} between the myelinated axons
587 to which γ parameters are sensitive, in at least two ways: first, decreasing the value of the magnetic
588 susceptibility of axons compared to that of the surrounding tissues and thus inducing a decreased
589 $\Delta\chi$; second, inducing a more prominent averaging effect of the diffusion on the inhomogeneities

590 induced by $\Delta\chi$ by increasing the space between the axons (Mitchell et al. 2010; Di Pietro et al.
591 2014). The overall effect would thus be a decrease in the magnitude of internal gradients g_{int} with a
592 consequent increase in γ .

593 Our speculations may be supported by other studies using different MRI techniques. For example,
594 the decrease in magnetization transfer (MT) is associated with loss of macromolecular content,
595 typically myelin. Two different studies (Dragansky et al., 2011, Callaghan et al., 2014) using a
596 quantitative MT approach to study brain aging, showed regional patterns of decreased MT similar to
597 those observed in our voxel-wise analysis of $M\gamma$ and γ_{\perp} .

598 Neither kurtosis nor DTI, and NODDI metrics showed significant correlations with age within the
599 genu and the anterior corona radiata, suggesting the complementarity of the γ metrics compared to
600 the other dMRI metrics in these regions.

601

602 **4.1.2 ODI increase and $D_{//}$ associated to axonal loss**

603 The present study also found a significant age-related decrease in $D_{//}$ as well as an increase in ODI
604 within the cerebral peduncle (CER), bilaterally, on a ROI-based analysis. The same significant
605 trends were found in the voxel-based analysis within the left CER and left IC_P. Other studies using
606 a TBSS approach on DTI-derived maps reported similar correlations of $D_{//}$ in the IC_P (Kawaguchi
607 et al., 2010) and both in the CER and the IC_P (Burzynska et al., 2010). In a study using both
608 NODDI and standard DTI metrics, Billet et al. (Billiet et al., 2015) reported a similar pattern of
609 decreased $D_{//}$ and an increased ODI with aging in these regions. However, this decrease was not
610 statistically significant.

611 This pattern of changes could reflect microscopic aging processes different from those described in
612 the previous section. However, in order to form a hypothesis about the microscopic modifications
613 causing these parameter changes, it is useful to understand the anatomical composition of the IC_P
614 and the CER. These regions are mainly formed by three fiber tracts: the corticospinal, the
615 corticobulbar and the corticopontine. These tracts are components of the projection fibers
616 interconnecting cortical areas with deep nuclei, brain stem, cerebellum and spinal cord. They
617 originate in the cerebral cortex and converge through the corona radiata to form the IC_P in a
618 tightly compact bundle, oriented in a superior-inferior direction. Subsequently, the fibers enter the
619 cerebral peduncle and continue their ways toward different destinations (Jellison et al., 2004).
620 Supposing that the projection fibers are markedly affected by aging, a lowered axial diffusivity may
621 be explained by axonal degeneration processes. Indeed, the beginning of the degeneration is
622 characterized by accumulation of organelles, such as lysosomes and mitochondria, as well as an
623 increase in neurofilament density within the axoplasm, thus hindering water molecule diffusion

624 along the axons (Peters, 2009, Peters and Kemper, 2012). Furthermore, the axons undergo
625 dystrophic changes such as swelling and beading, which have been shown to induce a reduction in
626 $D_{//}$ (Budde and Frank, 2010; Palombo et al. 2017). The space left empty by damaged fibers would
627 thus be occupied by crossing fibers less affected by aging, such as the fibers of the pontocerebellar
628 tract in the cerebral peduncle (Kamali et al., 2010) and those of the corticothalamic tract in the IC_P
629 (Axer and v Keyserlingk, 2000), thus contributing to a decrease in axial diffusivity and explaining
630 the parallel increase in orientation dispersion.

631 **4.1.3 WM modifications in the context of neurodegenerative theories**

632 The results obtained in the cortical RTZs as well as those obtained in the genu of corpus callosum
633 and the corona radiata are in line with the hypothesis of posterior-anterior gradient of degeneration.
634 The greatest correlation between parameters and age was found near the frontal lobe of the cortical
635 RTZs. The decrease in FA, and MK in frontal WM as well as the increase in ODI are coherent with
636 previous studies and the complementary increase in $M \gamma$ and γ_{\perp} with aging well fit a scenario of
637 decreased microstructural complexity, driven by axonal loss and demyelination.

638 The results obtained in the CER and the IC_P are coherent with the Wallerian hypothesis
639 suggesting that axonal degradation can contribute to the overall degenerating age-related process.

640 Neither our results nor the interpretations that we are proposing are in open contradiction with the
641 retrogenesis hypothesis. The genu is known to myelinate later than other fibers, while the CER and
642 the IC_P that are early myelinating fibers (Kinney et al., 1988, Label et al., 2008), undergo a
643 degeneration process different from demyelination.

644

645 **4.2 Microstructural variations in subcortical gray matter**

646

647 In scGM structures we observed a not uniform pattern of parametric correlation with aging,
648 possibly revealing regional-specific microscopic modifications.

649 **4.2.1 The putamen**

650 From a microscopic point of view, the putamen has a relatively simple structure. It is composed by
651 neurons with a thickly spherical arborization, which is densely covered with dendritic spines
652 (Yelnik, 2002). Nonetheless, in this region we found the strongest association between parameters
653 and age. All parameters correlated with age, apart from ODI: MD, axial and radial diffusivity as
654 well as $M \gamma$, axial and radial γ decreased, whereas all the other metrics increased. These results are

655 in general agreement with those reported in literature. The increase in FA associated with a decrease
656 in MD has been reported (Bhagat and Beaulieu, 2004, Abe et al., 2008, Pfefferbaum et al., 2010, Xu
657 et al., 2015). Specifically, the increase in FA has been associated with a higher decrease in D_{\perp} ,
658 compared with a more preserved value of D_{\parallel} (Wang et al., 2010). However, the microscopic
659 changes that drive these parameter modifications are still unclear. Some authors observed how they
660 could be related to the volume reduction of the striatum, with concurrent gliosis and tissue
661 compaction (Wang et al., 2010). Other authors argued that iron deposition may significantly affect
662 the measurement of water diffusion in the brain (Pfefferbaum et al., 2010, Xu et al., 2015). Indeed,
663 it is well established that a progressive iron deposition selectively affects scGM (Hallgren and
664 Sourander, 1958; Schipper, 2004, Acosta-Cabronero et al., 2016) and that the putamen presents the
665 strongest age-related increase (Acosta-Cabronero et al., 2016).

666 Our recent study of healthy young human brain (Caporale et al., 2017) suggested that γ -metrics is
667 sensitive to non-heme iron concentration, especially in sub-cortical GM. The results obtained in
668 scGM reported in the present study, are in good agreement with these previous findings. Indeed, the
669 marked negative trend of $M\gamma$, γ_{\parallel} and γ_{\perp} as a function of age in the putamen may reflect an increasing
670 effect of susceptibility inhomogeneities due to age-related iron accumulation.

671 According to the literature, an age-related increase in MK within the putamen has been found
672 (Gong et al. 2014). Dependence of the DKI derived metrics on the magnetic field inhomogeneities
673 has already been pointed out (Palombo et al. 2015), so it is likely that the correlation found between
674 the metrics derived by fitting data from the higher b-shells and aging are influenced by the iron
675 deposition. This is corroborated also by the observation that the shared variance between metrics
676 changes when considering WM and scGM. Specifically, in the latter case there is an increase in the
677 variance shared by metrics obtained from the higher b-shells, whereas there is a loss of shared
678 variance between DTI metrics and the others. γ metrics showed a higher correlation with age
679 compared to MK, this is likely due to the higher b-values used. These metrics are likely to be more
680 sensitive to iron deposition. It remains to be understood to what extent these changes are influenced
681 by microscopic changes and to what extent they are caused by local changes in the internal gradient.
682 More studies are required to clarify this issue.

683

684 **4.2.2 The thalamus**

685 The thalamus is the center through which patterns of nerve tracts from cerebral cortex and
686 subcortical and cerebellar regions connect. From a cytoarchitectonical point of view, it is divided

687 into numerous nuclei, each of which reflects a different functional connection with the cortex.
688 Several studies have reported a generalized age-related volume decrease (Raz et al., 2005,
689 Cherubini et al., 2009, Hughes et al., 2012), and it has been observed that some of the subregions
690 undergo differential shape changes with aging, including the anterior, the ventroanterior and the
691 dorsomedial nuclei (Hughes et al., 2012). DTI studies have reported an increase in MD along with a
692 non-significant decrease in FA using both a ROI-based (Cherubini et al., 2009, Hughes et al., 2012,
693 Gong et al., 2014) and a voxel-based approach (Draganski et al., 2011). Also, Gong *et al.* observed
694 a decrease in MK (Gong et al., 2014), but there is no study assessing the association between
695 NODDI parameters and age within the thalamus in the literature. Our results did not highlight MK
696 correlation with age, while they showed a decreased orientation dispersion using both the ROI-
697 based and the voxelwise-based approach as well as an increased axial diffusivity only in the ROI-
698 based approach. The voxelwise results showed a bilateral pattern of ODI increase that is more
699 accentuated in the left thalamus. The most affected regions seem to be the ventro-lateral and ventro-
700 anterior nuclei belonging to the so-called lateral group as well as some nuclei of the medial group
701 such as the center median and parafascicular groups, as defined by Morel *et al.* Microscopically
702 these regions are characterized by a higher concentration of myelinated fibers (Morel et al., 1997,
703 Danos et al., 2003). It has been established that, with aging, the dendritic tree undergoes a
704 progressive regression in GM, implying the reduction in number and length of the branches and the
705 decrease in the number of spines (Scheibel et al., 1975, Nakamura et al., 1985, Dumitriu et al.,
706 2010). In a recent study, comparing histology derived parameters and NODDI derived parameters
707 on spinal cord lesions from patients with multiple sclerosis, it has been shown that ODI well
708 matched its histology counterpart and, furthermore, that a lower ODI in the lesions was indicative of
709 reduced neurite architecture complexity (Grussu et al., 2017). Thus, regression of the dendritic tree
710 combined with relatively unaffected thalamic fibers would cause reduced neurite dispersion as well
711 as increased axial diffusivity, since the extra axonal water would be less hindered along the
712 direction of the fibers. Another possible explanation could be a selective degradation of some fiber
713 bundles.

714 **4.3 Interpretation of the NODDI parameter modifications with aging**

715 We found several associations between NODDI parameters and aging in different brain regions.
716 However, the interpretation of this correlation could be somehow tricky. A recent study showed that
717 some NODDI constraints seemed to be invalid (Lampinen et al., 2017). This inconsistency does not
718 hinder the model from fitting the data, especially in WM and thus the reported associations are
719 thought to be reliable. However, the interpretations of the parameters could be misleading. This

720 should be particularly true for the v_{in} and v_{fw} parameters, while ODI is supposed to be negligibly
721 affected (Zhang et al., 2012, Lampinen et al., 2017).

722

723 **4.4 Methodological considerations**

724 Although the studied cohort of subjects covered a broad age range, the total number of volunteers
725 recruited for the present study was smaller compared to other studies focused on aging (Callaghan
726 et al., 2014, Gong et al., 2014, Billet et al. 2015, Cox et a., 2016, Kodiweera et al. 2016). However,
727 our findings related to DTI, NODDI and MK metrics are broadly in accordance with those
728 presented in previous studies of larger cohorts (Billet et al. 2015, Kodiweera et al. 2016, Gong et al.,
729 2014).

730 In this study we assessed association between diffusion metrics and aging using a simple linear
731 regression. Other similar studies suggested that age-related changes follow non-linear trajectories
732 (Billet et al., 2015, Cox et al., 2016). However strong deviations from linear trends have been
733 primarily observed in different age ranges such as in brain maturation (Chang et al., 2015) or
734 including elderly subjects (Cox et al., 2016). Moreover, we found that linear regression well
735 described the trends observed in our data. Further studies involving more and older subjects, (>60y)
736 are needed to investigate higher order differences of γ -metrics with age.

737 Inadequate signal to noise ratio (SNR) can bias diffusion parameter estimation. To validate the
738 reliability of the quantified metrics, we investigated the SNR of our raw DW data as a function of
739 the b-values in WM and scGM (supplementary materials). We found that SNR was above the
740 critical value SNR=3. This should ensure an unbiased quantification of the diffusion metrics
741 obtained using higher b-values (Caporale et., al 2017, Jones et al., 2013).

742 Despite the quantification of γ -metrics requires the acquisition of images with b values higher than
743 those used to obtain DTI, DKI and NODDI metrics, the γ -metrics maps seem to be characterized by
744 a lower contrast to noise ratio than the maps reconstructed with the other metrics. This could affect
745 the accuracy and sensitivity of the technique. However, it should be considered that γ -derived maps
746 are showing different kind of information compared to that of conventional diffusion methods,
747 which apparently varies less across tissues.

748

749 This study suggests the ability of γ -metrics to detect age-related differences due to changes in $\Delta\chi$ -
750 driven inhomogeneities. Future studies should corroborate the results of the present study, possibly
751 using other specific quantitative MRI techniques such as quantitative susceptibility mapping (QSM)

752 or magnetization transfer (MT) to compare our technique with the two most common techniques
753 used for quantification of iron deposition and myelin content.

754 The long scanning time required by the diffusion protocol used in this study limits the amount of
755 different acquisitions and it is one of the major issues linked to the achievement of γ -weighted
756 maps. Therefore, the use of performing scanners with parallel acquisition mode is necessary to carry
757 out this type of investigation involving multi-b-value acquisitions. In supplementary materials, the
758 results of a preliminary study investigating the feasibility of using a down sampled protocol (with a
759 halved number of b-values and the same number of directions) are reported. Our preliminary results
760 in supplementary materials show that a protocol with a higher number of b-acquisitions, such as the
761 one used in this study, helps to reduce the variability in the γ extraction and in the bias introduced
762 when using the DTI reference frame approximation to extract the relevant γ -metrics according to De
763 Santis et al. (De Santis et al., 2011). However, the results also showed that by using a reduced
764 number of acquisitions it is still possible to obtain a reliable quantification of γ . Further studies are
765 needed to obtain the best tradeoff between an optimized protocol and reliable maps.

766 In this study we presented several associations between diffusion metrics and age. These
767 correlations don't necessarily imply a causal relationship. It is possible that other factors, such as
768 technical differences between different metrics, alter the sensitivity or accuracy of the fitting to the
769 data. This could potentially mean that the differences in correlations identified in the results are not
770 necessarily related to the ability of the techniques to identify different ageing mechanisms. Further
771 studies are necessary to confirm the conclusions of the present work.

772

773

774 **5 Conclusion**

775 In this study we used DTI, NODDI, MK and γ -metrics to assess physiological (i.e. the iron content)
776 and microstructural (myelin damage, axonal disintegration, neuron cell loss) changes in cerebral
777 WM and scGM of middle- and older-aged subjects. We found that γ -metrics are remarkably
778 sensitive and provide more complementary information than DTI-metrics, MK and NODDI in the
779 detection of frontal changes in the WM. The combined use of these techniques may also reveal
780 different patterns of age-related changes.

781

782 This study suggests that an increase in γ_{\perp} values within WM may reflect myelin degradation, and a
783 decrease in $M\gamma$ within scGM, specifically in the putamen, may reflect iron deposit accumulations.
784 Changes in $D_{//}$ and ODI could be indices of axon degradation in the pyramidal tract while reflecting

785 decreased architecture complexity within the thalamus. This study demonstrates the added value of
786 γ -metrics for assessing microscopic brain alterations due to aging and providing independent
787 measurements that are complementary to the conventional diffusion metrics. In conclusion, γ -
788 metrics combined with other DW-derived metrics can more comprehensively characterize the
789 complex mechanisms underlining age-related changes than conventional diffusion techniques alone.

790

791

792 **Funding sources**

793 This research did not receive any specific grant from funding agencies in the public, commercial, or
794 non-profit sectors.

795 **Resource data for this article**

796 The data belongs to a larger research project and we are not allowed to share it.

797 **References**

- 798 [Abe et al., 2002] Abe, O., Aoki, S., Hayashi, N., Yamada, H., Kunimatsu, A., Mori, H.,
799 Yoshikawa, T., Okubo, T., and Ohtomo, K. (2002). Normal aging in the central nervous system:
800 quantitative mr diffusion-tensor analysis. *Neurobiology of aging*, 23(3):433–441.
- 801 [Abe et al., 2008] Abe, O., Yamasue, H., Aoki, S., Suga, M., Yamada, H., Kasai, K., Masutani, Y.,
802 Kato, N., Kato, N., and Ohtomo, K. (2008). Aging in the cns: comparison of gray/white matter
803 volume and diffusion tensor data. *Neurobiology of aging*, 29(1):102–116.
- 804 [Acosta-Cabronero et al., 2016] Acosta-Cabronero, J., Betts, M. J., Cardenas-Blanco, A., Yang, S.,
805 and Nestor, P. J. (2016). In vivo mri mapping of brain iron deposition across the adult lifespan.
806 *Journal of Neuroscience*, 36(2):364–374.
- 807 [Andresson and Sotiropoulos 2016] Andersson, J. L. R. and Sotiropoulos, S. N. (2016). An
808 integrated approach to correction for off-resonance effects and subject movement in diffusion
809 MR imaging. *NeuroImage*, 125:1063-1078, 2016.
- 810 [Ardekani et al., 2007] Ardekani, S., Kumar, A., Bartzokis, G., and Sinha, U. (2007). Exploratory
811 voxel-based analysis of diffusion indices and hemispheric asymmetry in normal aging. *Magnetic
812 resonance imaging*, 25(2):154–167.
- 813 [Ashraf et al., 2018] Ashraf, A., Clark, M., and So, P.-W. (2018). The aging of iron man. *Frontiers
814 in aging neuroscience*, 10:65.

- 815 [Axe and v Keyserlingk, 2000] Axer, H. and v Keyserlingk, D. G. (2000). Mapping of fiber
816 orientation in human internal capsule by means of polarized light and confocal scanning laser
817 microscopy. *Journal of neuroscience methods*, 94(2):165–175.
- 818 [Bai et al., 2016] Bai, Y., Lin, Y., Tian, J., Shi, D., Cheng, J., Haacke, E.M., Hong, X., Ma, B.,
819 Zhou, J., Wang, M., (2016). Grading of Gliomas by Using Monoexponential, Biexponential,
820 and Stretched Exponential Diffusion-weighted MR Imaging and Diffusion Kurtosis MR
821 Imaging. *Radiology* 278, 496-504.
822
- 823 [Bartzokis et al., 2012] Bartzokis, G., Lu, P. H., Heydari, P., Couvrette, A., Lee, G. J., Kalashyan,
824 G., Freeman, F., Grinstead, J. W., Villablanca, P., Finn, J. P., et al. (2012). Multimodal
825 magnetic resonance imaging assessment of white matter aging trajectories over the lifespan of
826 healthy individuals. *Biological psychiatry*, 72(12):1026–1034.
- 827 [Basser et al., 1994] Basser, P. J., Mattiello, J., and LeBihan, D. (1994). Mr diffusion tensor
828 spectroscopy and imaging. *Biophysical journal*, 66(1):259–267.
- 829 [Bennet et al., 2003] Bennett, K.M., Schmainda, K.M., Bennett, R.T., Rowe, D.B., Lu, H., Hyde,
830 J.S., 2003. Characterization of continuously distributed cortical water diffusion rates with a
831 stretched-exponential model. *Magn Reson Med* 50, 727-734.
- 832 [Bhagat and Beaulieu, 2004] Bhagat, Y. A. and Beaulieu, C. (2004). Diffusion anisotropy in
833 subcortical white matter and cortical gray matter: Changes with aging and the role of csf-
834 suppression. *Journal of Magnetic Resonance Imaging*, 20(2):216–227.
- 835 [Billiet et al., 2015] Billiet, T., Vandenbulcke, M., Mädler, B., Peeters, R., Dhollander, T., Zhang,
836 H., Deprez, S., Van den Bergh, B. R., Sunaert, S., and Emsell, L. (2015). Age-related
837 microstructural differences quantified using myelin water imaging and advanced diffusion mri.
838 *Neurobiology of aging*, 36(6):2107–2121.
- 839 [Bowley et al., 2010] Bowley, M. P., Cabral, H., Rosene, D. L., and Peters, A. (2010). Age changes
840 in myelinated nerve fibers of the cingulate bundle and corpus callosum in the rhesus monkey.
841 *Journal of Comparative Neurology*, 518(15):3046–3064.
- 842 [Budde and Frank, 2010] Budde, M. D. and Frank, J. A. (2010). Neurite beading is sufficient to
843 decrease the apparent diffusion coefficient after ischemic stroke. *Proceedings of the National
844 Academy of Sciences*, 107(32):14472–14477.
- 845 [Burzynska et al., 2010] Burzynska, A. Z., Preuschhof, C., Bäckman, L., Nyberg, L., Li, S.C.,
846 Lindenberger, U., and Heekeren, H. R. (2010). Age-related differences in white matter
847 microstructure: region-specific patterns of diffusivity. *Neuroimage*, 49(3):2104–2112.
- 848 [Callaghan et al., 2014] Callaghan, M. F., Freund, P., Draganski, B., Anderson, E., Cappelletti,
849 M., Chowdhury, R., Diedrichsen, J., FitzGerald, T. H., Smittenaar, P., Helms, G., et al. (2014).
850 Widespread age-related differences in the human brain microstructure revealed by quantitative
851 magnetic resonance imaging. *Neurobiology of aging*, 35(8):1862–1872.

- 852 [Caporale et al., 2017] Caporale, A., Palombo, M., Macaluso, E., Guerreri, M., Bozzali, M., and
853 Capuani, S. (2017). The γ -parameter of anomalous diffusion quantified in human brain by mri
854 depends on local magnetic susceptibility differences. *Neuroimage*, 147:619–631.
- 855 [Capuani et al., 2013] Capuani, S., M. Palombo, A. Gabrielli, A. Orlandi, B. Maraviglia and F. S.
856 Pastore (2013). Spatio-temporal anomalous diffusion imaging: results in controlled phantoms
857 and in excised human meningiomas. *Magnetic resonance imaging* 31(3): 359-365.
858 doi:310.1016/j.mri.2012.1008.1012.
- 859 [Chang et al., 2015] Chang, Y. S., Owen, J. P., Pojman, N. J., Thieu, T., Bukshpun, P., Wakahiro,
860 M. L., Berman, J. I., Roberts, T. P., Nagarajan, S. S., Sherr, E. H., et al. (2015). White matter
861 changes of neurite density and fiber orientation dispersion during human brain maturation.
862 *PloS one*, 10(6):e0123656.
- 863 [Cherubini et al., 2009] Cherubini, A., Péran, P., Caltagirone, C., Sabatini, U., and Spalletta, G.
864 (2009). Aging of subcortical nuclei: microstructural, mineralization and atrophy modifications
865 measured in vivo using mri. *Neuroimage*, 48(1):29–36.
- 866 [Coutu et al. 2014] Coutu, J. P., Chen, J. J., Rosas, H. D., & Salat, D. H. (2014). Non-Gaussian
867 water diffusion in aging white matter. *Neurobiology of aging*, 35(6), 1412-1421.
- 868 [Cox et al., 2016] Cox, S. R., Ritchie, S. J., Tucker-Drob, E. M., Liewald, D. C., Hagenaars, S. P.,
869 Davies, G., Wardlaw, J. M., Gale, C. R., Bastin, M. E., and Deary, I. J. (2016). Ageing and
870 brain white matter structure in 3,513 uk biobank participants. *Nature communications*,
871 7:13629.
- 872 [Damoiseaux et al., 2009] Damoiseaux, J. S., Smith, S. M., Witter, M. P., Sanz- Arigita, E. J.,
873 Barkhof, F., Scheltens, P., ... & Rombouts, S. A. (2009). White matter tract integrity in aging
874 and Alzheimer's disease. *Human brain mapping*, 30(4), 1051-1059.
- 875 [Danos et al., 2003] Danos, P., Baumann, B., Krämer, A., Bernstein, H.-G., Stauch, R., Krell, D.,
876 Falkai, P., and Bogerts, B. (2003). Volumes of association thalamic nuclei in schizophrenia: a
877 postmortem study. *Schizophrenia Research*, 60(2-3):141–155.
- 878 [Daugherty and Raz, 2015] Daugherty, A. M. and Raz, N. (2015). Appraising the role of iron in
879 brain aging and cognition: promises and limitations of mri methods. *Neuropsychology review*,
880 25(3):272–287.
- 881 [Davis et al., 2009] Davis, S. W., Dennis, N. A., Buchler, N. G., White, L. E., Madden, D. J., &
882 Cabeza, R. (2009). Assessing the effects of age on long white matter tracts using diffusion
883 tensor tractography. *Neuroimage*, 46(2), 530-541.
- 884 [De Santis et al., 2011] De Santis, S., Gabrielli, A., Bozzali, M., Maraviglia, B., Macaluso, E.,
885 and Capuani, S. (2011a). Anisotropic anomalous diffusion assessed in the human brain by
886 scalar invariant indices. *Magnetic resonance in medicine*, 65(4):1043–1052.
- 887 [Di Pietro et al., 2014] Di Pietro, G., Palombo, M., Capuani, S. (2014) Internal Magnetic Field
888 Gradients in Heterogeneous Porous Systems: Comparison Between Spin-Echo and Diffusion
889 Decay Internal Field (DDIF) Method. *APPLIED MAGNETIC RESONANCE* 45(8)771-784

- 890 [Destainville 2008] Destainville, N., Saulière, A., Salomé, L. (2008). Comment to the article by
891 Michael J. Saxton: A biological interpretation of transient anomalous subdiffusion. I.
892 Qualitative model. *Biophysical Journal* 95: 3117-3119.
- 893 [Draganski et al., 2011] Draganski, B., Ashburner, J., Hutton, C., Kherif, F., Frackowiak, R. S.,
894 Helms, G., and Weiskopf, N. (2011). Regional specificity of mri contrast parameter changes in
895 normal ageing revealed by voxel-based quantification (vbq). *Neuroimage*, 55(4):1423–1434.
- 896 [Dubois et al., 2014] Dubois, J., Dehaene-Lambertz, G., Kulikova, S., Poupon, C., Hüppi, P. S.,
897 and Hertz-Pannier, L. (2014). The early development of brain white matter: a review of
898 imaging studies in fetuses, newborns and infants. *Neuroscience*, 276:48–71.
- 899 [Dumitriu et al., 2010] Dumitriu, D., Hao, J., Hara, Y., Kaufmann, J., Janssen, W. G., Lou, W.,
900 Rapp, P. R., and Morrison, J. H. (2010). Selective changes in thin spine density and
901 morphology in monkey prefrontal cortex correlate with aging-related cognitive impairment.
902 *Journal of Neuroscience*, 30(22):7507–7515.
- 903 [GadElkarim et al. 2013] GadElkarim, J. J., Magin, R. L., Meerschaert, M. M., Capuani, S.,
904 Palombo, M., Kumar, A., Leow, A. D. (2013) Fractional order generalization of anomalous
905 diffusion as a multidimensional extension of the transmission line equation. *IEEE Journal on*
906 *Emerging and Selected Topics in Circuits and Systems* 3(3):432-441.
- 907 [Giorgio et al., 2010] Giorgio, A., Santelli, L., Tomassini, V., Bosnell, R., Smith, S., De Stefano,
908 N., and Johansen-Berg, H. (2010). Age-related changes in grey and white matter structure
909 throughout adulthood. *Neuroimage*, 51(3):943–951.
- 910
- 911 [Gong et al., 2014] Gong, N.-J., Wong, C.-S., Chan, C.-C., Leung, L.-M., and Chu, Y.-C. (2014).
912 Aging in deep gray matter and white matter revealed by diffusional kurtosis imaging.
913 *Neurobiology of aging*, 35(10):2203–2216.
- 914 [Grussu et al., 2017] Grussu, F., Schneider, T., Tur, C., Yates, R. L., Tachrount, M., Ianaş, A.,
915 Yiannakas, M. C., Newcombe, J., Zhang, H., Alexander, D. C., et al. (2017). Neurite
916 dispersion: a new marker of multiple sclerosis spinal cord pathology? *Annals of clinical and*
917 *translational neurology*, 4(9):663–679.
- 918 [Haacke et al., 2010] Haacke, E. M., Miao, Y., Liu, M., Habib, C. A., Katkuri, Y., Liu, T., Yang,
919 Z., Lang, Z., Hu, J., and Wu, J. (2010). Correlation of putative iron content as represented by
920 changes in $r2^*$ and phase with age in deep gray matter of healthy adults. *Journal of Magnetic*
921 *Resonance Imaging*, 32(3):561–576.
- 922 [Hall and Barrick 2012] Hall, M. G. and T. R. Barrick (2012). Two- step anomalous diffusion
923 tensor imaging. *NMR in biomedicine* 25(2): 286-294. doi:210.1002/nbm.1747.
- 924 [Hallgren and Sourander, 1958] Hallgren, B. and Sourander, P. (1958). The effect of age on the
925 nonhaemin iron in the human brain. *Journal of neurochemistry*, 3(1):41–51.

- 926 [Hansen et al., 2013] Hansen, B., Lund, T. E., Sangill, R., & Jespersen, S. N. (2013).
927 Experimentally and computationally fast method for estimation of a mean kurtosis. *Magnetic*
928 *resonance in medicine*, 69(6), 1754-1760.
- 929 [Hermoye et al., 2006] Hermoye, L., Saint-Martin, C., Cosnard, G., Lee, S.-K., Kim, J.,
930 Nassogne, M.-C., Menten, R., Clapuyt, P., Donohue, P. K., Hua, K., et al. (2006). Pediatric
931 diffusion tensor imaging: normal database and observation of the white matter maturation in
932 early childhood. *Neuroimage*, 29(2):493–504.
- 933 [Hughes et al., 2012] Hughes, E. J., Bond, J., Svrckova, P., Makropoulos, A., Ball, G., Sharp, D.
934 J., Edwards, A. D., Hajnal, J. V., and Counsell, S. J. (2012). Regional changes in thalamic
935 shape and volume with increasing age. *Neuroimage*, 63(3):1134–1142.
- 936 [Ingo et al 2014] Ingo, C., R. L. Magin, L. Colon- Perez, W. Triplett and T. H. Mareci (2014).
937 On random walks and entropy in diffusion- weighted magnetic resonance imaging studies of
938 neural tissue. *Magnetic resonance in medicine* 71(2): 617-627. doi:610.1002/mrm.24706.
- 939 [Jelescu and Budde, 2017] Jelescu, I. O. and Budde, M. D. (2017). Design and validation of
940 diffusion mri models of white matter. *Frontiers in Physics*, 5:61.
- 941 [Jellison et al., 2004] Jellison, B. J., Field, A. S., Medow, J., Lazar, M., Salamat, M. S., and
942 Alexander, A. L. (2004). Diffusion tensor imaging of cerebral white matter: a pictorial review
943 of physics, fiber tract anatomy, and tumor imaging patterns. *American Journal of*
944 *Neuroradiology*, 25(3):356–369.
- 945 [Jensen et al. 2005] Jensen J.H., Helpert J.A., Ramani A., Lu H., Kaczynski K. (2005)
946 Diffusional kurtosis imaging: the quantification of non-gaussian water diffusion by means of
947 magnetic resonance imaging. *Magn Reson Med*. 53:1432–1440.
948
- 949 [Jensen et al. 2010] Jensen J.H. and Helpert J.A. (2010) MRI quantification of non-Gaussian
950 water diffusion by kurtosis analysis. *NMR Biomed*. 2010; 23: 698-710.
- 951 [Jones et al., 1999] Jones, D. K., Horsfield, M. A., and Simmons, A. (1999). Optimal strategies
952 for measuring diffusion in anisotropic systems by magnetic resonance imaging. *Magnetic*
953 *Resonance in Medicine: An Official Journal of the International Society for Magnetic*
954 *Resonance in Medicine*, 42(3):515–525.
- 955 [Jones et al., 2013] Jones, D. K., Knösche, T. R., & Turner, R. (2013). White matter integrity,
956 fiber count, and other fallacies: the do's and don'ts of diffusion MRI. *Neuroimage*, 73, 239-254.
- 957 [Kamali et al., 2010] Kamali, A., Kramer, L. A., Frye, R. E., Butler, I. J., and Hasan, K. M. (2010).
958 Diffusion tensor tractography of the human brain cortico-ponto-cerebellar pathways: A
959 quantitative preliminary study. *Journal of Magnetic Resonance Imaging*, 32(4):809–817.
- 960 [Karaman and Zhou 2018] Karaman M. M., Zhou X. J. (2018) A fractional motion diffusion
961 model for a twice- refocused spin- echo pulse sequence. *NMR Biomed* First published: 22
962 August 2018 <https://doi.org/10.1002/nbm.3960>

- 963 [Kawaguchi et al., 2010] Kawaguchi, H., Obata, T., Ota, M., Akine, Y., Ito, H., Ikehira, H.,
964 Kanno, I., and Suhara, T. (2010). Regional heterogeneity and age-related change in subregions
965 of internal capsule evaluated by diffusion tensor imaging. *Brain research*, 1354:30–39.
- 966 [Keihaninejad et al., 2013] Keihaninejad, S., Zhang, H., Ryan, N. S., Malone, I. B., Modat, M.,
967 Cardoso, M. J., Cash, D. M., Fox, N. C., and Ourselin, S. (2013). An unbiased longitudinal
968 analysis framework for tracking white matter changes using diffusion tensor imaging with
969 application to alzheimer’s disease. *Neuroimage*, 72:153–163.
- 970 [Kellner et al., 2016] Kellner, E., Dhital, B., Kiselev, V. G., and Reisert, M. (2016). Gibbs-
971 ringing artifact removal based on local subvoxel-shifts. *Magnetic resonance in medicine*,
972 76(5):1574–1581.
- 973 [Kingsley, 2006] Kingsley, P. B. (2006). Introduction to diffusion tensor imaging mathematics:
974 Part iii. tensor calculation, noise, simulations, and optimization. *Concepts in Magnetic*
975 *Resonance Part A*, 28(2):155–179.
- 976 [Kiselev, 2017] Kiselev, V. G. (2017). Fundamentals of diffusion mri physics. *NMR in*
977 *Biomedicine*, 30(3):e3602.
- 978 [Kodiweera et al., 2016] Kodiweera, C., Alexander, A. L., Harezlak, J., McAllister, T. W., and
979 Wu, Y.-C. (2016). Age effects and sex differences in human brain white matter of young to
980 middle-aged adults: a dti, nodd, and q-space study. *Neuroimage*, 128:180–192.
- 981 [Lai et al., 2015] Lai, V., Lee, V.H., Lam, K.O., Sze, H.C., Chan, Q., Khong, P.L., (2015).
982 Intravoxel water diffusion heterogeneity MR imaging of nasopharyngeal carcinoma using
983 stretched exponential diffusion model. *Eur Radiol* 25, 1708-1713.
- 984 [Lampinen et al., 2017] Lampinen, B., Szczepankiewicz, F., Mårtensson, J., van Westen, D.,
985 Sundgren, P. C., and Nilsson, M. (2017). Neurite density imaging versus imaging of
986 microscopic anisotropy in diffusion mri: A model comparison using spherical tensor encoding.
987 *NeuroImage*, 147:517–531.
- 988 [Landman et al., 2007] Landman, B. A., Farrell, J. A., Jones, C. K., Smith, S. A., Prince, J. L.,
989 and Mori, S. (2007). Effects of diffusion weighting schemes on the reproducibility of dti-
990 derived fractional anisotropy, mean diffusivity, and principal eigenvector measurements at 1.5
991 t. *Neuroimage*, 36(4):1123–1138.
- 992 [Langkammer et al., 2012] Langkammer, C., Schweser, F., Krebs, N., Deistung, A., Goessler, W.,
993 Scheurer, E., Sommer, K., Reishofer, G., Yen, K., Fazekas, F., et al. (2012). Quantitative
994 susceptibility mapping (qsm) as a means to measure brain iron? a post mortem validation
995 study. *Neuroimage*, 62(3):1593–1599.
- 996 [Lätt et al. 2013] Lätt, J., Nilsson, M., Wirestam, R., Ståhlberg, F., Karlsson, N., Johansson, M.,
997 ... & van Westen, D. (2013). Regional values of diffusional kurtosis estimates in the healthy
998 brain. *Journal of Magnetic Resonance Imaging*, 37(3), 610-618.
- 999 [Lin, 2015] Lin, G., (2015). An effective phase shift diffusion equation method for analysis of
1000 PFG normal and fractional diffusions. *J Magn Reson*

- 1001 [Lin, 2016] Lin, G., (2016). Instantaneous signal attenuation method for analysis of PFG
1002 fractional diffusions. *J Magn Reson*
- 1003 [Lin, 2018] Lin, G., (2018) General PFG signal attenuation expressions for anisotropic anomalous
1004 diffusion by modified-Bloch equations. *Physica A*, 497:86-100.
- 1005 [Liu, 2010] Liu, C. (2010). Susceptibility tensor imaging. *Magnetic Resonance in Medicine: An Official*
1006 *Journal of the International Society for Magnetic Resonance in Medicine*, 63(6):1471–1477.
- 1007 [Lockhart et al., 2014] Lockhart, S., DeCarli, C., and Fama, R. (2014). Neuroimaging of the aging
1008 brain: Introduction to the special issue of neuropsychology review.
- 1009 [Magin et al 2008] Magin, R. L., O. Abdullah, D. Baleanu and X. J. Zhou (2008). Anomalous
1010 diffusion expressed through fractional order differential operators in the Bloch–Torrey
1011 equation. *Journal of Magnetic Resonance* 190(2): 255-270.
1012 doi:210.1016/j.jmr.2007.1011.1007.
- 1013 [Mitchell et al., 2010] Mitchell, J., Chandrasekera, T.C., Johns, M.L., Gladden, L. F., Fordham,
1014 E.J., (2010) Nuclear magnetic resonance relaxation and diffusion in the presence of internal
1015 gradients: The effect of magnetic field strength *PHYSICAL REVIEW E* 81 (2) Article Number:
1016 026101
- 1017 [Metzler and Klafter 2000] Metzler R., Klafter J., (2000) The random walk's guide to anomalous
1018 diffusion: a fractional dynamics approach. *Phys. Rep.* 339, 1
- 1019 [Metzler et al. 2014] Metzler R, Jeon J-H, Cherstvy A G and Barkai E (2014) Anomalous
1020 diffusion models and their properties: non-stationarity, non-ergodicity, and ageing at the
1021 centenary of single particle tracking. *Phys.Chem. Chem. Phys.* 16, 24128.
- 1022 [Morel et al., 1997] Morel, A., Magnin, M., and Jeanmonod, D. (1997). Multiarchitectonic and
1023 stereotactic atlas of the human thalamus. *Journal of Comparative Neurology*, 387(4):588–630.
- 1024 [Mori et al., 2008] Mori, S., Oishi, K., Jiang, H., Jiang, L., Li, X., Akhter, K., Hua, K., Faria, A.
1025 V., Mahmood, A., Woods, R., et al. (2008). Stereotaxic white matter atlas based on diffusion
1026 tensor imaging in an icbm template. *Neuroimage*, 40(2):570–582.
- 1027 [Nakamura et al., 1985] Nakamura, S., Akiguchi, I., Kameyama, M., and Mizuno, N. (1985).
1028 Age-related changes of pyramidal cell basal dendrites in layers iii and v of human motor
1029 cortex: a quantitative golgi study. *Acta neuropathologica*, 65(3-4):281–284.
- 1030 [Nicholson 2015] Nicholson, C. (2015). Anomalous diffusion inspires anatomical insights.
1031 *Biophysical Journal* 108: 2091-2093.
- 1032 [Nilsson et al., 2012] Nilsson, M., Lätt, J., Ståhlberg, F., Westen, D., and Hagslätt, H. (2012). The
1033 importance of axonal undulation in diffusion mr measurements: a monte carlo simulation
1034 study. *NMR in Biomedicine*, 25(5):795–805.
- 1035 [Novikov et al., 2018] Novikov, D. S., Kiselev, V. G., and Jespersen, S. N. (2018). On modeling.
1036 *Magnetic resonance in medicine*, 79(6):3172–3193.

- 1037 [Palombo et al., 2011] Palombo, M., A. Gabrielli, S. De Santis, C. Cametti, G. Ruocco and S.
1038 Capuani (2011). Spatio-temporal anomalous diffusion in heterogeneous media by nuclear
1039 magnetic resonance. *The Journal of chemical physics* 135(3): 034504.
1040 doi:034510.031063/034501.3610367.
- 1041 [Palombo et al., 2012] Palombo, M., A. Gabrielli, S. De Santis and S. Capuani (2012). The γ
1042 parameter of the stretched-exponential model is influenced by internal gradients: validation in
1043 phantoms. *Journal of Magnetic Resonance* 216: 28-36. doi:10.1016/j.jmr.2011.1012.1023.
- 1044 [Palombo et al. 2015] Palombo, M., Gentili, S., Bozzali, M., Macaluso, E., & Capuani, S.
1045 (2015). New insight into the contrast in diffusional kurtosis images: Does it depend on
1046 magnetic susceptibility?. *Magnetic resonance in medicine*, 73(5), 2015-2024.
- 1047 [Palombo et al., 2017] Palombo, M., Ligneul, C., Hernandez-Garzon, E., & Valette, J. (2017).
1048 Can we detect the effect of spines and leaflets on the diffusion of brain intracellular
1049 metabolites?. *Neuroimage*. In press. DOI - 10.1016/j.neuroimage.2017.05.003.
- 1050 [Peters, 2009] Peters, A. (2009). The effects of normal aging on myelinated nerve fibers in
1051 monkey central nervous system. *Frontiers in neuroanatomy*, 3:11.
- 1052 [Peters and Kemper, 2012] Peters, A. and Kemper, T. (2012). A review of the structural
1053 alterations in the cerebral hemispheres of the aging rhesus monkey. *Neurobiology of aging*,
1054 33(10):2357–2372.
- 1055 [Pfefferbaum et al., 2000] Pfefferbaum, A., Sullivan, E. V., Hedehus, M., Lim, K. O.,
1056 Adalsteinsson, E., and Moseley, M. (2000). Age-related decline in brain white matter anisotropy
1057 measured with spatially corrected echo-planar diffusion tensor imaging. *Magnetic Resonance in*
1058 *Medicine: An Official Journal of the International Society for Magnetic Resonance in Medicine*,
1059 44(2):259–268.
- 1060 [Sullivan and Pfefferbaum, 2006] Sullivan, E. V., & Pfefferbaum, A. (2006). Diffusion tensor
1061 imaging and aging. *Neuroscience & Biobehavioral Reviews*, 30(6), 749-761.
- 1062 [Pfefferbaum et al., 2010] Pfefferbaum, A., Adalsteinsson, E., Rohlfing, T., and Sullivan, E. V.
1063 (2010). Diffusion tensor imaging of deep gray matter brain structures: effects of age and iron
1064 concentration. *Neurobiology of aging*, 31(3):482–493.
- 1065 [Pirpamer et al., 2016] Pirpamer, L., Hofer, E., Gesierich, B., De Guio, F., Freudenberger, P.,
1066 Seiler, S., Duering, M., Jouvent, E., Duchesnay, E., Dichgans, M., et al. (2016). Determinants
1067 of iron accumulation in the normal aging brain. *Neurobiology of aging*, 43:149–155.
- 1068 [Rathi et al., 2014] Rathi, Y., Pasternak, O., Savadjiev, P., Michailovich, O., Bouix, S., Kubicki,
1069 M., Westin, C.-F., Makris, N., and Shenton, M. E. (2014). Gray matter alterations in early
1070 aging: A diffusion magnetic resonance imaging study. *Human brain mapping*, 35(8):3841–
1071 3856.
- 1072 [Raz, 2000] Raz, N. (2000). Aging of the brain and its impact on cognitive performance:
1073 Integration of structural and functional findings.

- 1074 [Raz et al., 2005] Raz, N., Lindenberger, U., Rodrigue, K. M., Kennedy, K. M., Head, D.,
1075 Williamson, A., Dahle, C., Gerstorff, D., and Acker, J. D. (2005). Regional brain changes in
1076 aging healthy adults: general trends, individual differences and modifiers. *Cerebral cortex*,
1077 15(11):1676–1689.
- 1078 [Salat et al., 2005] Salat, D., Tuch, D., Greve, D., Van Der Kouwe, A., Hevelone, N., Zaleta, A.,
1079 Rosen, B., Fischl, B., Corkin, S., Rosas, H. D., et al. (2005). Age-related alterations in white
1080 matter microstructure measured by diffusion tensor imaging. *Neurobiology of aging*,
1081 26(8):1215–1227.
- 1082 [Salminen et al., 2016] Salminen, L. E., Conturo, T. E., Laidlaw, D. H., Cabeen, R. P., Akbudak,
1083 E., Lane, E. M., Heaps, J. M., Bolzenius, J. D., Baker, L. M., Cooley, S., et al. (2016). Regional
1084 age differences in gray matter diffusivity among healthy older adults. *Brain imaging and
1085 behavior*, 10(1):203–211.
- 1086 [Sandell and Peters, 2003] Sandell, J. H. and Peters, A. (2003). Disrupted myelin and axon loss in
1087 the anterior commissure of the aged rhesus monkey. *Journal of Comparative Neurology*,
1088 466(1):14–30.
- 1089 [Scheibel et al., 1975] Scheibel, M. E., Lindsay, R. D., Tomiyasu, U., and Scheibel, A. B.
1090 (1975). Progressive dendritic changes in aging human cortex. *Experimental neurology*,
1091 47(3):392–403.
- 1092 [Schipper, 2004] Schipper, H. M. (2004). Brain iron deposition and the free radical-mitochondrial
1093 theory of ageing. *Ageing research reviews*, 3(3):265–301.
- 1094 [Saxton, 2008] Saxton, M. J. (2008). Response to comment by Destainville et al. *Biophysical
1095 Journal* 95:3120-3122.
- 1096 [Simmonds et al., 2014] Simmonds, D. J., Hallquist, M. N., Asato, M., and Luna, B. (2014).
1097 Developmental stages and sex differences of white matter and behavioral development through
1098 adolescence: a longitudinal diffusion tensor imaging (dti) study. *Neuroimage*, 92:356–368.
- 1099 [Smith et al., 2006] Smith, S. M., Jenkinson, M., Johansen-Berg, H., Rueckert, D., Nichols, T. E.,
1100 Mackay, C. E., Watkins, K. E., Ciccarelli, O., Cader, M. Z., Matthews, P. M., et al. (2006).
1101 Tract-based spatial statistics: voxelwise analysis of multi-subject diffusion data. *Neuroimage*,
1102 31(4):1487–1505.
- 1103 [Striker et al., 2009] Stricker, N. H., Schweinsburg, B. C., Delano-Wood, L., Wierenga, C. E.,
1104 Bangen, K. J., Haaland, K. Y., ... & Bondi, M. W. (2009). Decreased white matter integrity in
1105 late-myelinating fiber pathways in Alzheimer's disease supports retrogenesis. *Neuroimage*, 45(1),
1106 10-16.
- 1107 [Sullivan et al., 2010] Sullivan, E. V., Rohlfing, T., and Pfefferbaum, A. (2010). Quantitative fiber
1108 tracking of lateral and interhemispheric white matter systems in normal aging: relations to timed
1109 performance. *Neurobiology of aging*, 31(3):464–481.

- 1110 [Timmers et al., 2016] Timmers, I., Roebroek, A., Bastiani, M., Jansma, B., Rubio-Gozalbo, E.,
1111 and Zhang, H. (2016). Assessing microstructural substrates of white matter abnormalities: a
1112 comparative study using dti and nodd. *PloS one*, 11(12):e0167884.
- 1113 [Tournier et al., 2012] Tournier, J.-D., Calamante, F., and Connelly, A. (2012). Mrtrix: diffusion
1114 tractography in crossing fiber regions. *International Journal of Imaging Systems and*
1115 *Technology*, 22(1):53–66.
- 1116 [Veraart et al., 2016a] Veraart, J., Fieremans, E., and Novikov, D. S. (2016a). Diffusion mri noise
1117 mapping using random matrix theory. *Magnetic resonance in medicine*, 76(5):1582–1593.
- 1118 [Veraart et al., 2016b] Veraart, J., Novikov, D. S., Christiaens, D., Ades-Aron, B., Sijbers, J., and
1119 Fieremans, E. (2016b). Denoising of diffusion mri using random matrix theory. *Neuroimage*,
1120 142:394–406.
- 1121 [Wang et al., 2010] Wang, Q., Xu, X., and Zhang, M. (2010). Normal aging in the basal ganglia
1122 evaluated by eigenvalues of diffusion tensor imaging. *American journal of neuroradiology*,
1123 31(3):516–520.
- 1124 [Wang et al., 2011] Wang, Y., Gupta, A., Liu, Z., Zhang, H., Escolar, M. L., Gilmore, J. H.,
1125 Gouttard, S., Fillard, P., Maltbie, E., Gerig, G., et al. (2011). Dti registration in atlas based fiber
1126 analysis of infantile krabbe disease. *Neuroimage*, 55(4):1577–1586.
- 1127 [Wheeler-Kingshott and Cercignani, 2009] Wheeler-Kingshott, C. A. and Cercignani, M. (2009).
1128 About “axial” and “radial” diffusivities. *Magnetic Resonance in Medicine: An Official Journal of*
1129 *the International Society for Magnetic Resonance in Medicine*, 61(5):1255–1260.
- 1130 [Xu et al., 2008] Xu, X., Wang, Q., and Zhang, M. (2008). Age, gender, and hemispheric
1131 differences in iron deposition in the human brain: an in vivo mri study. *Neuroimage*, 40(1):35–
1132 42.
- 1133 [Xu et al., 2015] Xu, X., Wang, Q., Zhong, J., and Zhang, M. (2015). Iron deposition influences
1134 the measurement of water diffusion tensor in the human brain: a combined analysis of diffusion
1135 and ironinduced phase changes. *Neuroradiology*, 57(11):1169–1178.
- 1136 [Yamada et al., 2014] Yamada, H., Abe, O., Shizukuishi, T., Kikuta, J., Shinozaki, T., Dezawa,
1137 K., Nagano, A., Matsuda, M., Haradome, H., and Imamura, Y. (2014). Efficacy of distortion
1138 correction on diffusion imaging: comparison of fsl eddy and eddy_correct using 30 and 60
1139 directions diffusion encoding. *PloS one*, 9(11):e112411.
- 1140 [Yelnik, 2002] Yelnik, J. (2002). Functional anatomy of the basal ganglia. *Movement disorders*,
1141 17(S3).
- 1142 [Yu et al. 2018] Yu Q., Reutens D., Vegh V. (2018) Can anomalous diffusion models in magnetic
1143 resonance imaging be used to characterise white matter tissue microstructure? *Neuroimage*
1144 *NeuroImage* 175:122-137.

- 1145 [Zhang et al., 2006] Zhang, H., Yushkevich, P. A., Alexander, D. C., and Gee, J. C. (2006).
1146 Deformable registration of diffusion tensor mr images with explicit orientation optimization.
1147 *Medical image analysis*, 10(5):764–785.
- 1148 [Zhang et al., 2010] Zhang, Y., Du, A.-T., Hayasaka, S., Jahng, G.-h., Hlavin, J., Zhan, W., Weiner,
1149 M. W., and Schuff, N. (2010). Patterns of age-related water diffusion changes in human brain by
1150 concordance and discordance analysis. *Neurobiology of aging*, 31(11):1991– 2001.
- 1151 [Zhang et al., 2012] Zhang, H., Schneider, T., Wheeler-Kingshott, C. A., and Alexander, D. C.
1152 (2012). Noddi: practical in vivo neurite orientation dispersion and density imaging of the
1153 human brain. *Neuroimage*, 61(4):1000–1016.
- 1154 [Zhou et al. 2010] Zhou, X.J., Gao, Q., Abdullah, O., Magin, R.L., (2010). Studies of anomalous
1155 diffusion in the human brain using fractional order calculus. *Magn. Reson. Med.* 63 (3), 562–
1156 569

9. Figure
[Click here to download high resolution image](#)

Volunteers: 32 subjects (Age range 20-77y Mean/SD = 44/18y)

Acquisition scheme: 11 b-shells with 15 directions each + b_0

a

Noise correction (*Dwidenoise-MRtrix3*)

Gibbs ringing correction (*Kellner et al.*)

Eddy current correction (*EDDY-FSL*)

b

b up to 1.5 ($\text{ms}/\mu\text{m}^2$)

b up to 2.5 ($\text{ms}/\mu\text{m}^2$)

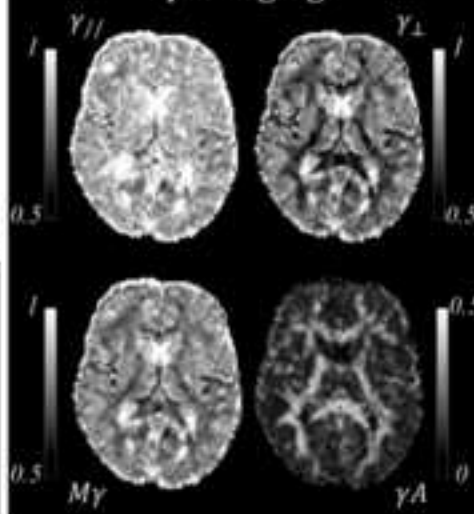
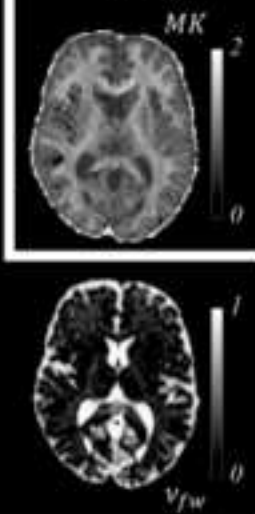
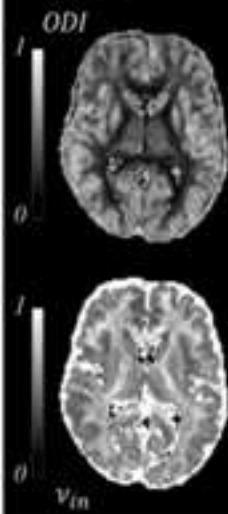
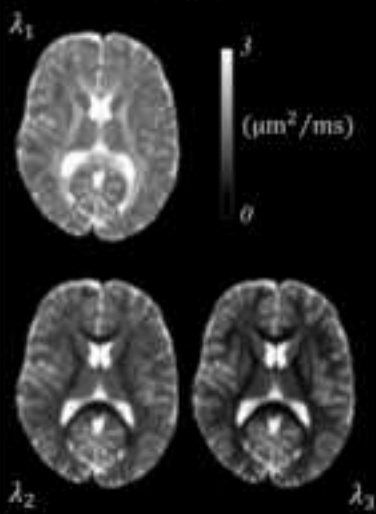
b up to 5.0 ($\text{ms}/\mu\text{m}^2$)

DTI

NODDI

DKI

γ -imaging



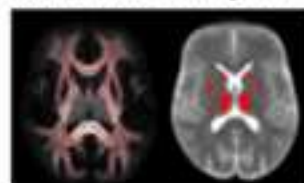
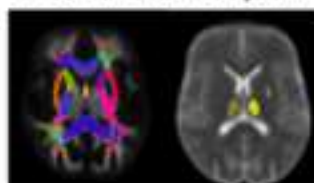
c

Spatial normalization (*DTI-TK*) + mean FA skeleton (*TBSS*)

Normalization and projection of the other parametric maps

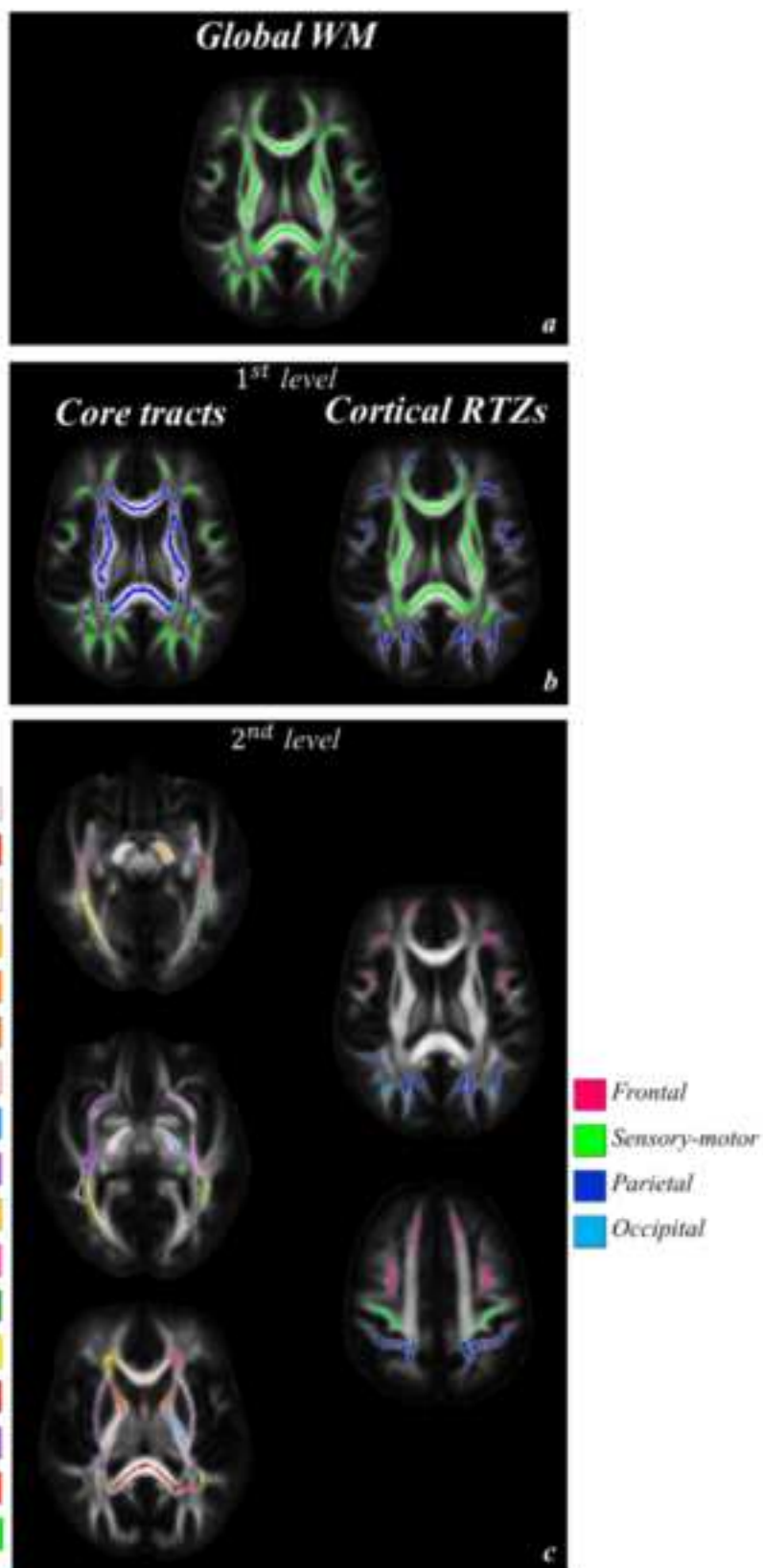
ROI-based analysis

Voxel-wise analysis

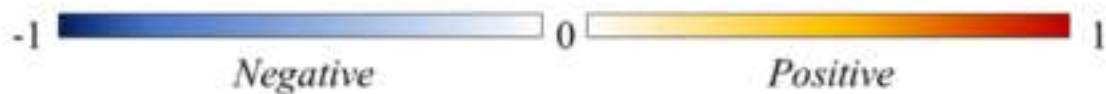
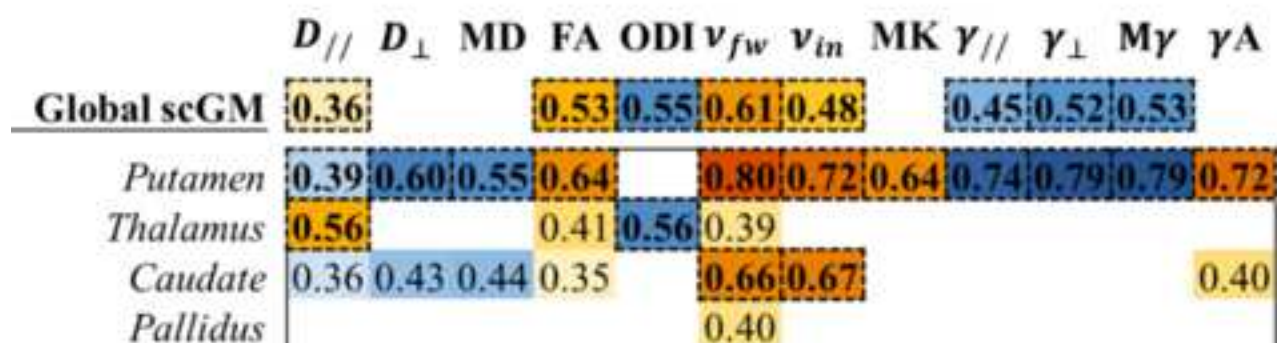
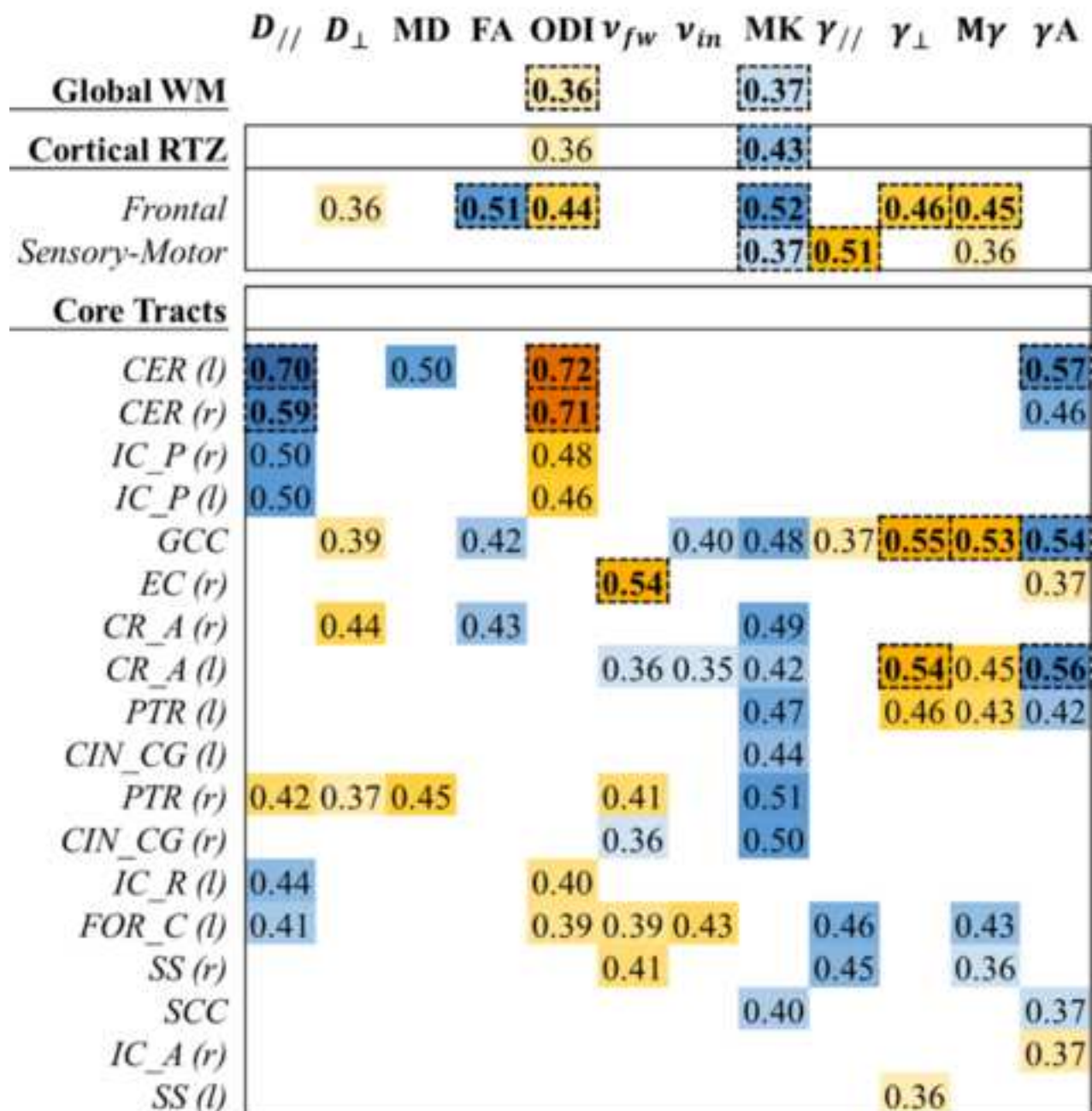


d

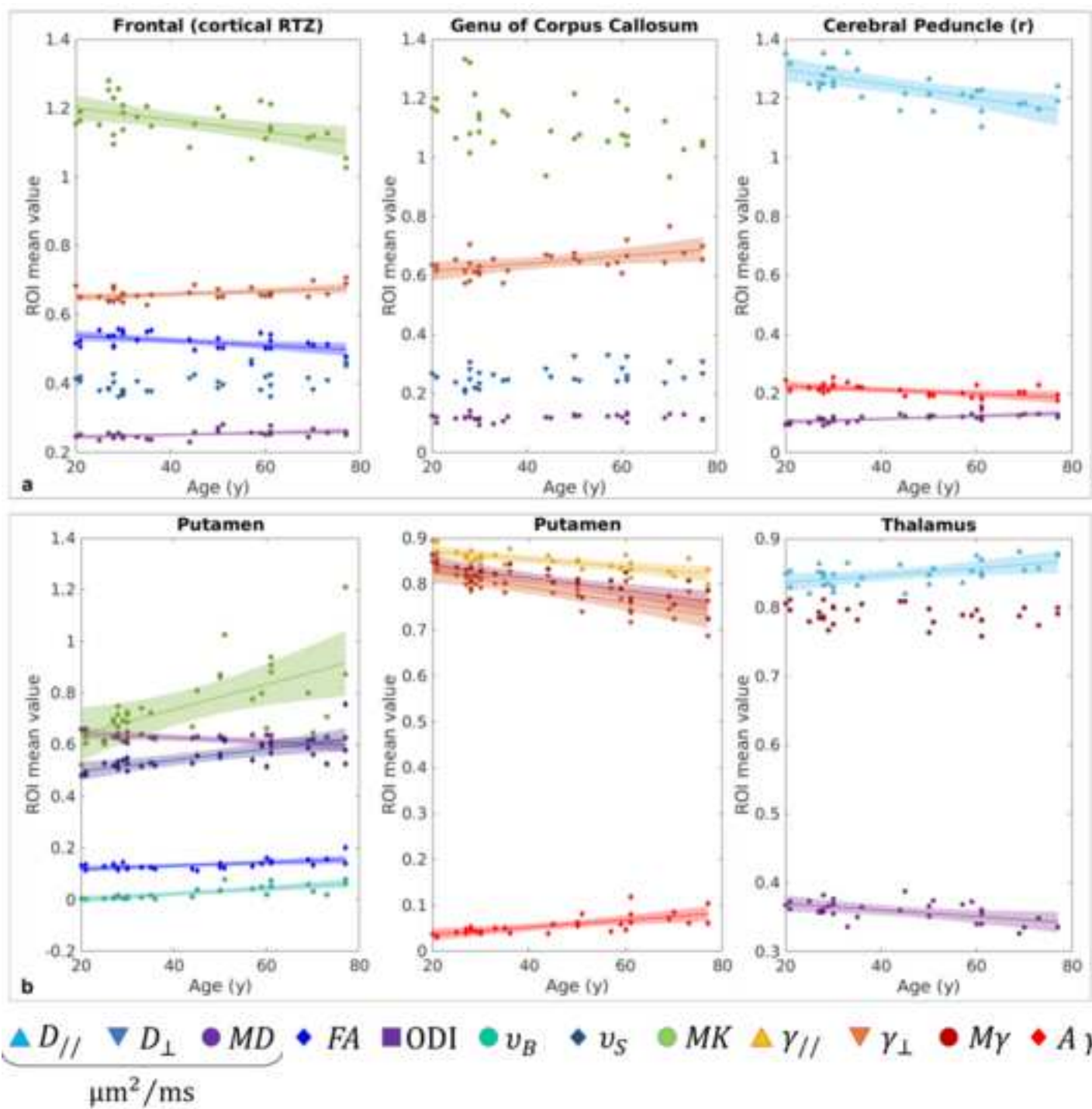
9. Figure
[Click here to download high resolution image](#)



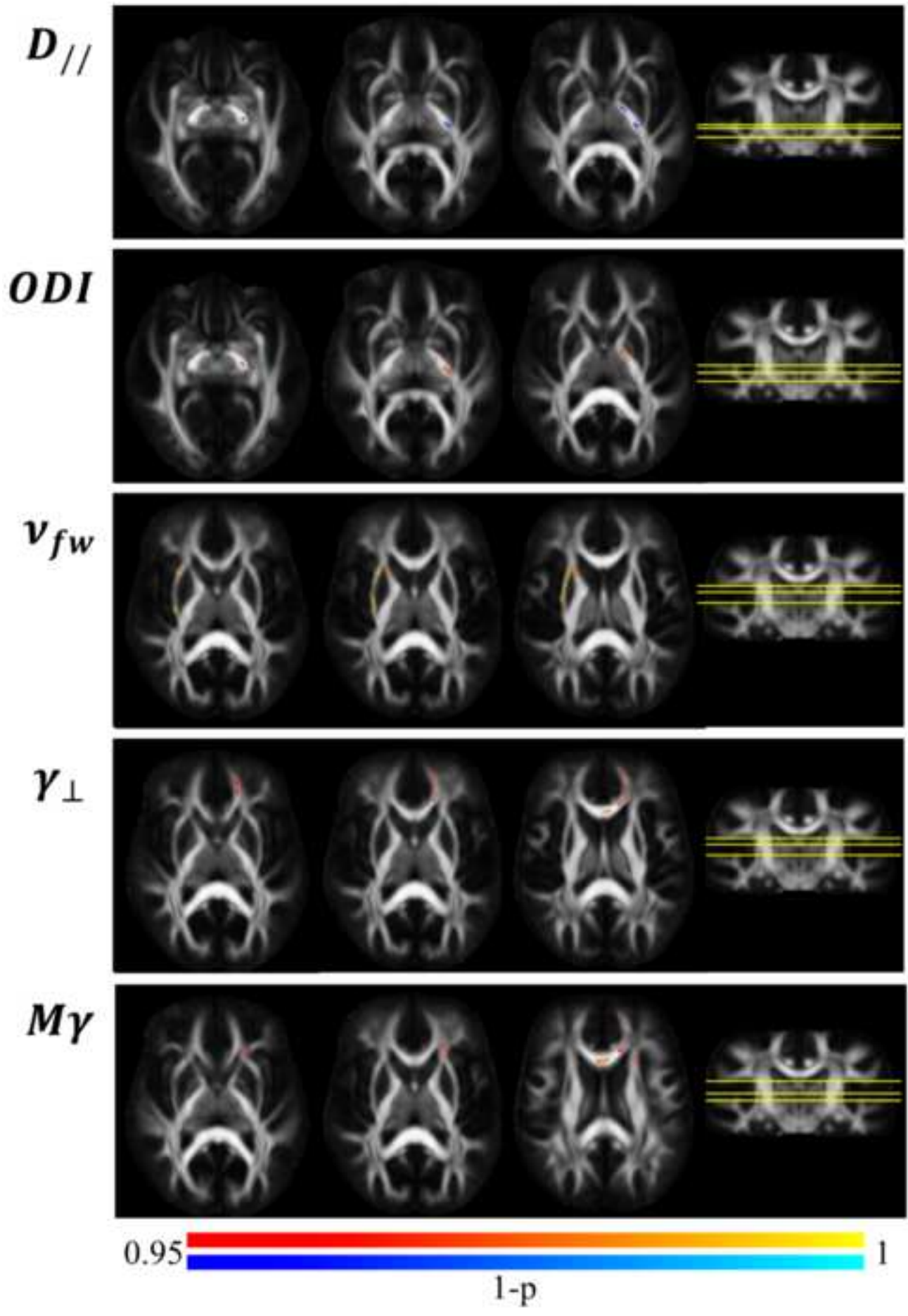
9. Figure
[Click here to download high resolution image](#)



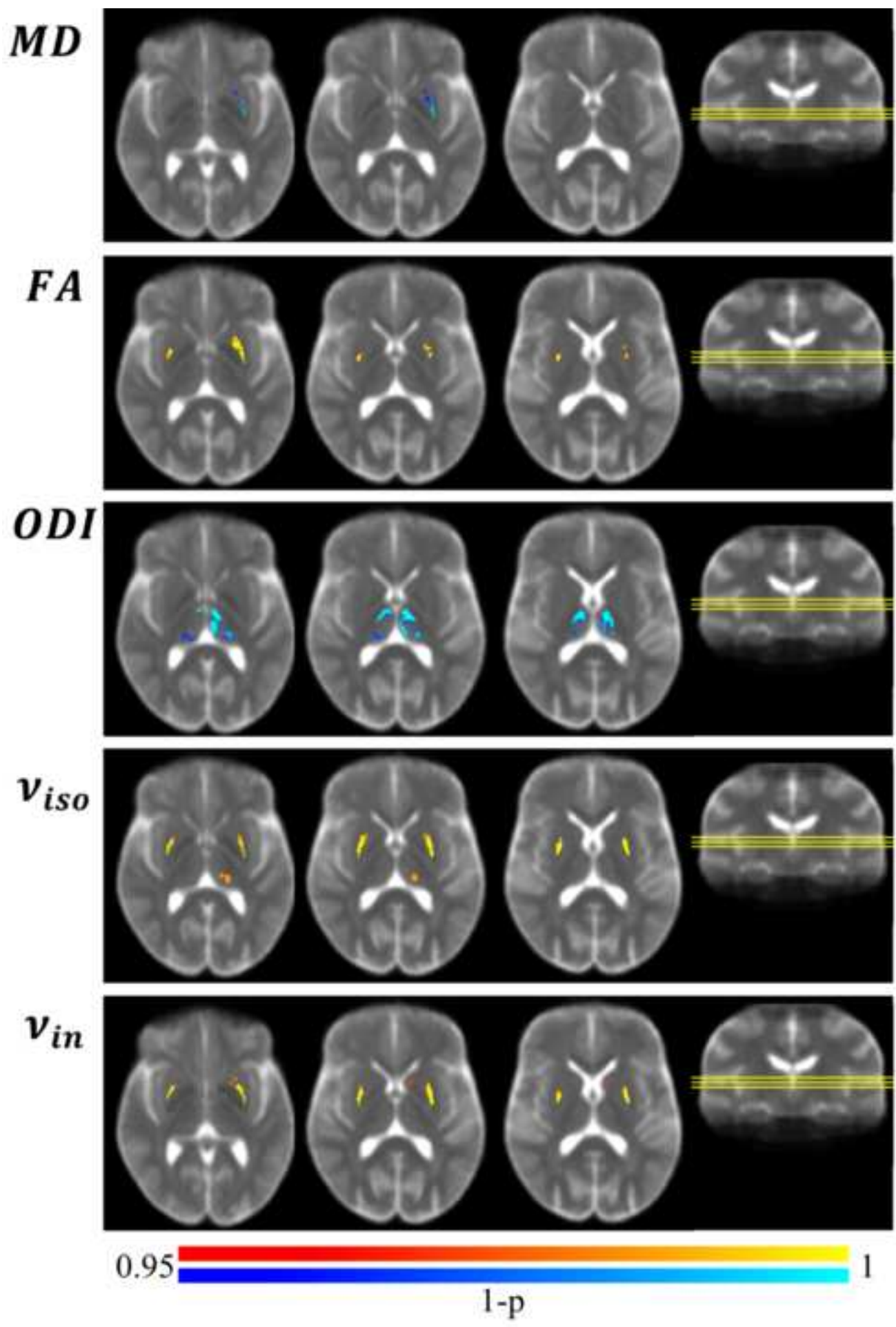
9. Figure
[Click here to download high resolution image](#)



9. Figure
[Click here to download high resolution image](#)

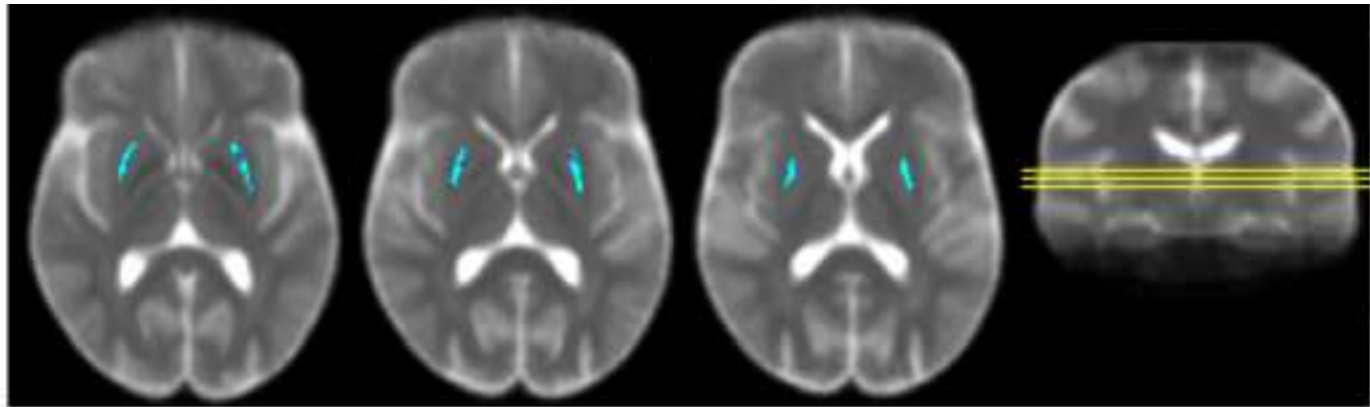


9. Figure
[Click here to download high resolution image](#)

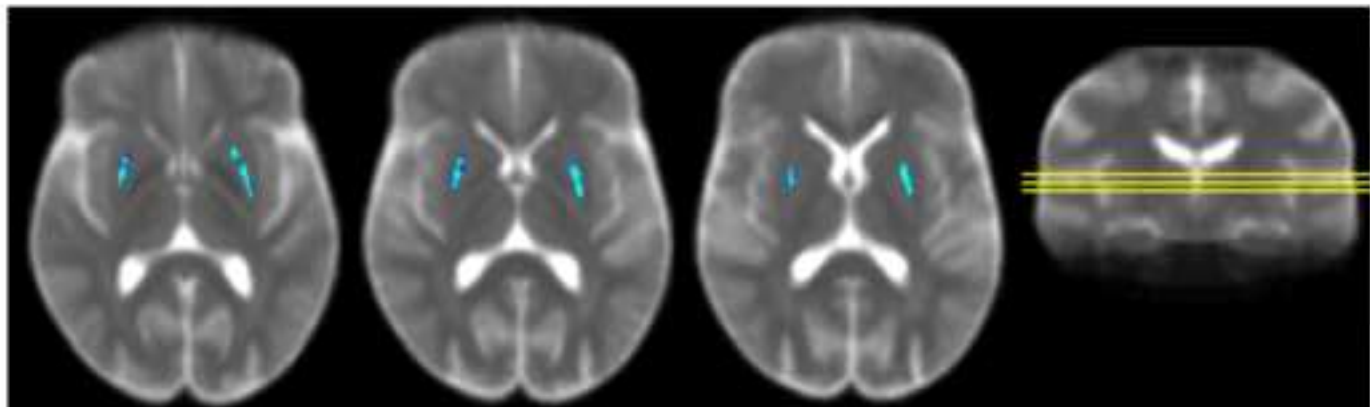


9. Figure
[Click here to download high resolution image](#)

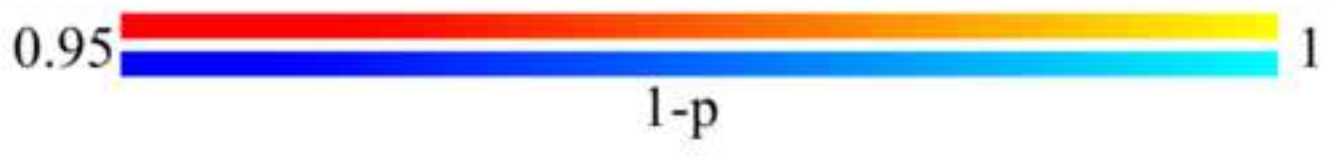
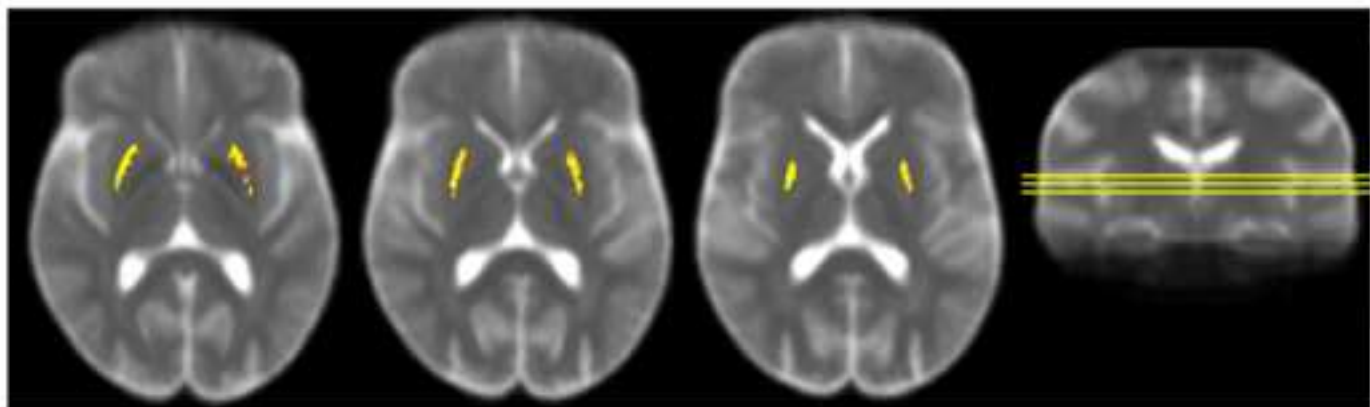
γ_{\perp}



$M\gamma$



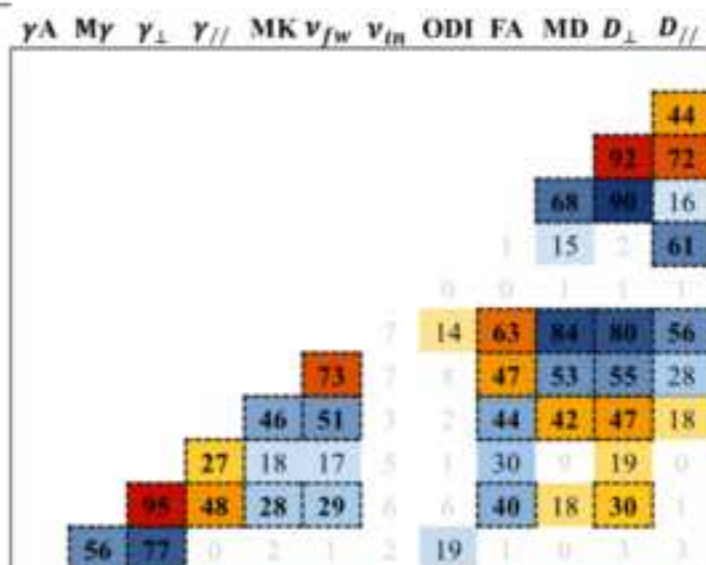
γ_A



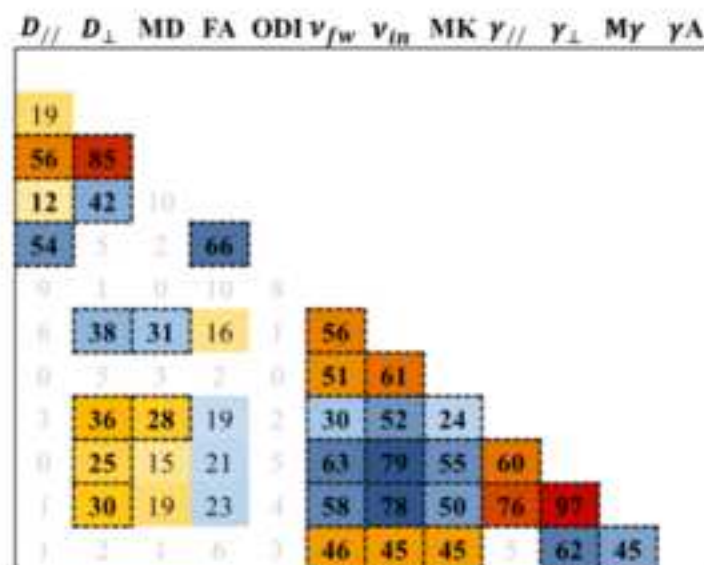
9. Figure

[Click here to download high resolution image](#)

Global WM



Global scGM



10. Supplementary Material

[Click here to download 10. Supplementary Material: SupplementaryMaterials.docx](#)

Resource data for this article

The data belongs to a larger research project and we are not allowed to share it.

We are happy to share the code for our γ -weighted maps on demand.